IMPLEMENTATION OF THE EQUIVALENCE PRINCIPLE ALGORITHM FOR POTENTIAL INTEGRAL EQUATIONS

A THESIS SUBMITTED TO
THE GRADUATE SCHOOL OF NATURAL AND APPLIED SCIENCES
OF
MIDDLE EAST TECHNICAL UNIVERSITY

BY

ALI FARSHKARAN

IN PARTIAL FULFILLMENT OF THE REQUIREMENTS
FOR
THE DEGREE OF MASTER OF SCIENCE
IN
ELECTRICAL AND ELECTRONICS ENGINEERING

JUNE 2018

Approval of the thesis:

IMPLEMENTATION OF THE EQUIVALENCE PRINCIPLE ALGORITHM FOR POTENTIAL INTEGRAL EQUATIONS

submitted by **ALI FARSHKARAN** in partial fulfillment of the requirements for the degree of **Master of Science in Electrical and Electronics Engineering Department, Middle East Technical University** by,

Prof. Dr. Prof. Dr. Halil Kalıpçılar
Dean, Graduate School of **Natural and Applied Sciences** _____

Prof. Dr. Tolga Çiloğlu
Head of Department, **Electrical and Electronics Engineering** _____

Assoc. Prof. Dr. Özgür Ergül
Supervisor, **Elec. and Electronics Eng. Dept., METU** _____

Examining Committee Members:

Prof. Dr. Sencer Koç
Electrical and Electronics Engineering Department, METU _____

Assoc. Prof. Dr. Özgür Ergül
Electrical and Electronics Engineering Department, METU _____

Prof. Dr. Özlem Aydın Çivi
Electrical and Electronics Engineering Department, METU _____

Assoc. Prof. Dr. Lale Alatan
Electrical and Electronics Engineering Department, METU _____

Prof. Dr. Vakur Behçet Ertürk
Elec. and Electronics Engineering Dept., Bilkent University _____

Date: _____

I hereby declare that all information in this document has been obtained and presented in accordance with academic rules and ethical conduct. I also declare that, as required by these rules and conduct, I have fully cited and referenced all material and results that are not original to this work.

Name, Last Name: Ali Farshkaran

Signature   :

ABSTRACT

**IMPLEMENTATION OF THE EQUIVALENCE PRINCIPLE ALGORITHM
FOR POTENTIAL INTEGRAL EQUATIONS**

Farshkaran, Ali

M.S., Department of Electrical and Electronics Engineering

Supervisor   : Assoc. Prof. Dr. Özgür Ergül

JUNE 2018, 59 pages

In this thesis, a domain decomposition method based on the Huygens' principle for integral equations is studied. Step-by-step development of equivalence principle algorithm (EPA) is described for solving arbitrary shaped perfect electric conductor (PEC) and penetrable objects. The main advantage of EPA is its efficiency thanks to the enhanced conditioning hence accelerated iterative solutions of the matrix equations derived from discretizations. For further enhancing the efficiency, the multilevel fast multipole algorithm (MLFMA) is used to speed up the matrix-vector multiplications (MVMs) in EPA. Following standard implementations, a novel implementation of EPA using potential integral equations (PIEs) is further presented. EPA is generalized to be compatible with PIEs used to formulate inner problems inside equivalence surfaces. Based on the stability of PIEs at low frequencies, the resulting EPA-PIE implementation is suitable for low-frequency problems involving dense discretizations with respect to wavelength. Along with the formulation and demonstration of the EPA-PIE scheme, high accuracy and stability of the implementation are presented on canonical problems.

ÖZ

POTANSİYEL İNTEGRAL DENKLEMLER İÇİN EŞDEĞERLİK PRENSİBİ ALGORİTMASININ UYGULANMASI

Farshkaran, Ali

Yüksek Lisans, Elektrik ve Elektronik Mühendisliği Bölümü

Tez Yöneticisi   : Doç. Dr. Özgür Ergül

Haziran 2018 , 59 sayfa

Bu tezde, integral denklemleri için Huygens prensibine dayalı bir alan ayrıştırma yöntemi incelenmiştir. Rastgele şekilli iletken yüzeylerin ve nüfuz edilebilir nesnelerin çözümü için eşdeğerlik prensibi algoritmasının (EPA) geliştirilmesi adım adım tarif edilmiştir. EPA'nın esas avantajı geliştirilmiş koşulluluğu sayesinde verimli olmasıdır ki, bu sayede ayrıklaştırmalardan türetilen matris denklemlerinin hızlandırılmış iteratif çözümleri elde edilebilir. Verimliliği daha da artırmak amacıyla, EPA'nın matris vektör çarpımlarını hızlandırmak için çok seviyeli hızlı çokkutup yöntemi (MLFMA) kullanılmıştır. Standart uygulamalardan sonra, potansiyel integral denklemlerinin (PIE) kullanıldığı özgün bir EPA uygulaması sunulmuştur. EPA, eşdeğer yüzeylerin içindeki iç problemleri formülleştirmek için kullanılan PIE'ler ile uyumlu olacak şekilde genelleştirilmiştir. PIE'lerin düşük frekanslardaki kararlılığı sayesinde, elde edilen EPA-PIE uygulaması dalga boyuna göre yoğun ayrıklaştırmalar içeren düşük frekans problemleri için uygundur. EPA-PIE uygulamasının formülasyonu ve gösterimi ile birlikte, kanonik problemler üzerindeki yüksek doğruluğu ve kararlılığı sunulmuştur.

Anahtar Kelimeler: Yüzey İntegral Denklemleri, Eşdeğerlik Prensibi Algoritması, Çok Seviyeli Hızlı Çokkutup Yöntemi, Potansiyel Formülasyonları

to my mother and father...

ACKNOWLEDGMENTS

TABLE OF CONTENTS

xii

LIST OF FIGURES

FIGURES

xiv

LIST OF ABBREVIATIONS

AD	Approximate diagonalization
CFIE	Combined-field integral equation
CTF	Combined tangential formulation
EFIE	Electric-field integral equation
EPA	Equivalence principle algorithm
ES	Equivalence surface
FMM	Fast multipole method
GMRES	Generalized minimal residual
IE	Integral equation
IO	Inside-out
JMCFIE	J and M (Electric and magnetic current) combined-field integral equation
LF	Low frequency
MCTF	Modified combined tangential field
MFIE	Magnetic-field integral equation
MoM	Method of moments
MLFMA	Multilevel fast multipole algorithm
OI	Outside-in
PDE	Partial differential equation
PEC	Perfect electric conductor
PIE	Potential integral equation
PMCHWT	Poggio–Miller–Chang–Harrington–Wu–Tsai
RCS	Radar cross section
RFID	Radio frequency identification
RWG	Rao-Wilton-Glisson
SIE	Surface integral equation
SRR	Split-ring resonator

CHAPTER 1

INTRODUCTION

Nowadays, with the help of computer technology, computational modeling has become very important in electromagnetics, especially when dealing with problems that are not easily handled with analytical or experimental methods. Numerical methods used in computational electromagnetics can be divided into partial differential equation (PDE) and integral equation (IE) methods. Unlike PDE methods that employ volumetric discretizations of problems, IE methods can be applied by discretizing object surfaces, leading to surface integral equations (SIEs) that require fewer unknowns in comparison to other methods. Due to their advantages, SIEs are widely used for scattering and radiation problems involving large geometries. SIEs can be cast into matrix equations using the method of moments (MoM). Beside its advantages, there are various challenges while using MoM. As a major one, when the problem size grows, the memory and time cost of the solution increases rapidly. As a remedy for this, different efficient algorithms, such as the fast multipole method (FMM) or its extended version, i.e., the multilevel fast multipole algorithm (MLFMA), have been developed in order to decrease the complexity of solutions [1,2]. These algorithms are based on iterative solutions of matrix equations. However, ill conditioning of matrix equations may result in very poor convergence rates or even convergence to incorrect solutions that makes these algorithms inefficient and/or unstable. Even though some formulations result in well-conditioned matrix equations, there is a threshold between accuracy and conditioning [3]. Preconditioning can be used to improve effective conditioning of matrix equations. However, preconditioners are commonly specific to the problem and formulation so that their implementations may not be generalized. Another problem arises in case of dense discretizations, as in MoM solutions of SIEs, especially when the mesh size becomes very small with respect to wavelength due to

fine geometric details. Dense discretizations further deteriorate the conditioning, often leading to non-convergent solutions. This problem is known as the low-frequency breakdown and it appears both in the formulations and in the context of fast solvers, such as MLFMA.

In this thesis, we focus on the equivalence principle algorithm (EPA), which is a well-known domain decomposition method for integral-equation-based solvers [4, 5]. In EPA, the problem domain is divided into subdomains and each subdomain is enclosed by an equivalence surface (ES). Then, Huygens' principle is employed in order to replace the original unknowns in each subdomain to new unknowns on the surrounding ES. For each subdomain, surface-integral-equation formulations can be used, while the electromagnetic interactions between subdomains are calculated via ESs. In general, EPA has a noticeable efficiency in solving finite or infinite array structures with identical elements, such as antenna arrays [6–8] and metamaterials [9]. In these cases, by considering identical ESs, the solution mechanism is the same for all subdomains. On the other side, hybridization of EPA with asymptotic and fast methods is also possible [10, 11]. Due to the nature of matrix equations created by EPA, the conditioning is always very well and iterative solutions can converge much faster than those in the ordinary MoM formulations.

As a domain decomposition method, solving multiscale problems is one of the main applications for EPA. However, similar to the other surface-integral-equation methods, EPA suffers from low-frequency breakdowns, which are inherently related to the applied formulations in subdomains, for fine discretizations of structures and ESs. A main track for solving the low-frequency breakdown in surface formulations is to separate contributions of the magnetic vector potential and the electric scalar potential. Recently, potential integral equations (PIEs) have been introduced as a remedy for low-frequency breakdown in surface formulations [12–17]. In PIEs, boundary conditions for the vector and scalar potentials are enforced on the surface of the given scatterer. It has been shown that PIEs do not suffer from any breakdown even at extremely low frequencies (small objects/discretizations), provided that they are supported by appropriate post processing [16], making them very suitable for low-frequency problems. In this thesis, we present a robust implementation of EPA-PIE, i.e., a novel combination of an EPA solver and a PIE formulation, for solving challenging low-frequency and multiscale problems.

2
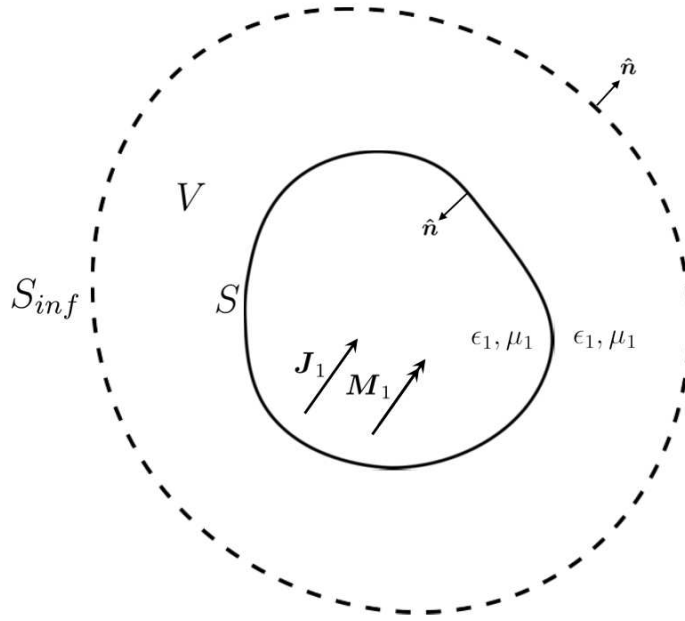
Figure 1.1: Geometry used for the derivation of Huygens' principle.

In the rest of this chapter, equivalence principle and SIE concepts are discussed. Later, a brief discussion of MoM implementations is presented. In Chapter 2, development of EPA for PEC and penetrable objects is explained. In the third Chapter, acceleration of EPA using MLFMA and numerical results for large array structures are presented. EPA operators have been modified in Chapter 4 in order to be compatible with PIEs. Finally, the EPA-PIE implementation is demonstrated and its stability is shown on canonical objects.

1.1 Huygens' Principle

Huygens' principle states that electromagnetic fields out of a surface S enclosing a source region can be expressed in terms of fields on S. Referring to Figure 1.1, in region V, the electric field satisfies source-free vector wave equation

$$\nabla \times \nabla \times \boldsymbol{E}(\boldsymbol{r}) - k^2 \boldsymbol{E}(\boldsymbol{r}) = 0, \tag{1.1}$$

in the frequency domain using $\exp(-i\omega t)$ time convention. Also, the dyadic Green's function satisfies

$$\nabla \times \nabla \times \bar{\boldsymbol{G}}(\boldsymbol{r}, \boldsymbol{r}') - k^2 \bar{\boldsymbol{G}}(\boldsymbol{r}, \boldsymbol{r}') = \bar{\boldsymbol{I}}\delta(\boldsymbol{r} - \boldsymbol{r}'), \tag{1.2}$$

where

$$\bar{\boldsymbol{G}}(\boldsymbol{r}, \boldsymbol{r}') = \left[\bar{\boldsymbol{I}} + \frac{\nabla\nabla}{k^2}\right] g(\boldsymbol{r}, \boldsymbol{r}') \tag{1.3}$$

and

$$g(\boldsymbol{r}, \boldsymbol{r}') = \frac{\exp(ik|\boldsymbol{r} - \boldsymbol{r}'|)}{4\pi|\boldsymbol{r} - \boldsymbol{r}'|}. \tag{1.4}$$

Here, k is the wavenumber, and $\boldsymbol{r}'$ and $\boldsymbol{r}$ represent source and observation points, respectively. By applying the vector Green's theorem, the electric field in V can be expressed as

$$\boldsymbol{E}(\boldsymbol{r}') = -\int_S dS \left[i\omega\mu\hat{\boldsymbol{n}} \times \boldsymbol{H}(\boldsymbol{r}) \cdot \bar{\boldsymbol{G}}(\boldsymbol{r}, \boldsymbol{r}') + \hat{\boldsymbol{n}} \times \boldsymbol{E}(\boldsymbol{r}) \cdot \nabla \times \bar{\boldsymbol{G}}(\boldsymbol{r}, \boldsymbol{r}')\right]. \tag{1.5}$$

Equation 1.5 indicates that, knowing the tangential components of electric and magnetic fields on S, fields outside S can be calculated. The tangential components of the fields can be considered as equivalent current distributions as

$$\boldsymbol{J}(\boldsymbol{r}) = \hat{\boldsymbol{n}} \times \boldsymbol{H}(\boldsymbol{r}) \tag{1.6}$$

$$\boldsymbol{M}(\boldsymbol{r}) = -\hat{\boldsymbol{n}} \times \boldsymbol{E}(\boldsymbol{r}). \tag{1.7}$$

1.2 Surface Integral Equations

Before discussing SIEs, we consider frequency-domain Maxwell equations for a linear, isotropic, and homogeneous medium, given as

$$\nabla \times \boldsymbol{E}(\boldsymbol{r}) = i\omega\mu\boldsymbol{H}(\boldsymbol{r}) - \boldsymbol{M}(\boldsymbol{r}) \tag{1.8}$$

$$\nabla \times \boldsymbol{H}(\boldsymbol{r}) = -i\omega\epsilon\boldsymbol{E}(\boldsymbol{r}) + \boldsymbol{J}(\boldsymbol{r}) \tag{1.9}$$

$$\nabla \cdot \boldsymbol{E}(\boldsymbol{r}) = \frac{1}{\epsilon}\rho_e(\boldsymbol{r}) \tag{1.10}$$

$$\nabla \cdot \boldsymbol{H}(\boldsymbol{r}) = \frac{1}{\mu}\rho_m(\boldsymbol{r}), \tag{1.11}$$

4

where current and charge densities satisfy continuity equations as

$$\nabla \cdot \boldsymbol{J}(\boldsymbol{r}) = i\omega \rho_e(\boldsymbol{r}) \tag{1.12}$$

$$\nabla \cdot \boldsymbol{M}(\boldsymbol{r}) = i\omega \rho_m(\boldsymbol{r}). \tag{1.13}$$

Employing the potential theory [18], electric and magnetic fields can be derived as

$$\boldsymbol{E}(\boldsymbol{r}) = i\omega\mu \int d\boldsymbol{r}' \left[\boldsymbol{J}(\boldsymbol{r}') + \frac{1}{k^2}\nabla' \cdot \boldsymbol{J}(\boldsymbol{r}')\nabla \right] g(\boldsymbol{r}, \boldsymbol{r}')$$

$$- \int d\boldsymbol{r}'\nabla g(\boldsymbol{r}, \boldsymbol{r}') \times \boldsymbol{M}(\boldsymbol{r}') \tag{1.14}$$

$$\boldsymbol{H}(\boldsymbol{r}) = i\omega\epsilon \int d\boldsymbol{r}' \left[\boldsymbol{M}(\boldsymbol{r}') + \frac{1}{k^2}\nabla' \cdot \boldsymbol{M}(\boldsymbol{r}')\nabla \right] g(\boldsymbol{r}, \boldsymbol{r}')$$

$$+ \int d\boldsymbol{r}'\nabla g(\boldsymbol{r}, \boldsymbol{r}') \times \boldsymbol{J}(\boldsymbol{r}'). \tag{1.15}$$

Equations (1.14) and (1.15) are solutions of Helmholtz equations for arbitrary source distributions $\boldsymbol{J}$ and $\boldsymbol{M}$ within a homogeneous medium with parameters ϵ and μ. At this stage, it is more convenient to use integro-differential operators defined as

$$\boldsymbol{\mathcal{L}}\{\boldsymbol{X}\}(\boldsymbol{r}) = ik \int d\boldsymbol{r}' \left[\boldsymbol{X}(\boldsymbol{r}') + \frac{1}{k^2}\nabla' \cdot \boldsymbol{X}(\boldsymbol{r}')\nabla \right] g(\boldsymbol{r}, \boldsymbol{r}') \tag{1.16}$$

$$\boldsymbol{\mathcal{K}}\{\boldsymbol{X}\}(\boldsymbol{r}) = \int d\boldsymbol{r}'\boldsymbol{X}(\boldsymbol{r}') \times \nabla'g(\boldsymbol{r}, \boldsymbol{r}'), \tag{1.17}$$

as well as the identity operator

$$\boldsymbol{\mathcal{I}}\{\boldsymbol{X}\}(\boldsymbol{r}) = \boldsymbol{X}(\boldsymbol{r}). \tag{1.18}$$

Then, equations (1.14) and (1.15) can be expressed in simpler forms as

$$\boldsymbol{E}(\boldsymbol{r}) = \eta\boldsymbol{\mathcal{L}}\{\boldsymbol{J}\}(\boldsymbol{r}) - \boldsymbol{\mathcal{K}}\{\boldsymbol{M}\}(\boldsymbol{r}) \tag{1.19}$$

$$\boldsymbol{H}(\boldsymbol{r}) = \eta^{-1}\boldsymbol{\mathcal{L}}\{\boldsymbol{M}\}(\boldsymbol{r}) + \boldsymbol{\mathcal{K}}\{\boldsymbol{J}\}(\boldsymbol{r}), \tag{1.20}$$

where η is the intrinsic impedance. In order to derive IEs, we consider a homogeneous region D_u with parameters ϵ_u and μ_u bounded by surface S_u. The equivalent current sources can be defined as $\boldsymbol{J}_u = \hat{\boldsymbol{n}} \times \boldsymbol{H}_u$ and $\boldsymbol{M}_u = -\hat{\boldsymbol{n}} \times \boldsymbol{E}_u$, where $\boldsymbol{E}_u$ and $\boldsymbol{H}_u$ represent total electric and magnetic fields. For the electric field, one can write

$$-\boldsymbol{M}_u(\boldsymbol{r}) = \hat{\boldsymbol{n}}_u \times \boldsymbol{E}_u(\boldsymbol{r})$$

$$= \hat{\boldsymbol{n}}_u \times \boldsymbol{E}_u^i(\boldsymbol{r}) + \hat{\boldsymbol{n}}_u \times \boldsymbol{E}_u^s(\boldsymbol{r}) \tag{1.21}$$

$$= \hat{\boldsymbol{n}}_u \times \boldsymbol{E}_u^i(\boldsymbol{r}) + \hat{\boldsymbol{n}}_u \times \eta_u\boldsymbol{\mathcal{L}}_u\{\boldsymbol{J}_u\}(\boldsymbol{r}) - \hat{\boldsymbol{n}}_u \times \boldsymbol{\mathcal{K}}_u\{\boldsymbol{M}_u\}(\boldsymbol{r}),$$

where $\mathcal{L}_u$ and $\mathcal{K}_u$ are the integro-differential operators associated with region D_u, $\hat{n}_u$ represents inward unit normal, and η_u is the intrinsic impedance of the region. The operator $\mathcal{K}_u$ has a hypersingular kernel $\nabla g_u(\boldsymbol{r}, \boldsymbol{r}')$. This hypersingularity can be handled by extracting the limit part of $\mathcal{K}_u$ as $\boldsymbol{r} \to \boldsymbol{r}'$, i.e.,

$$\mathcal{K}_u\{\boldsymbol{X}\}(\boldsymbol{r}) = \mathcal{K}_u^{PV}\{\boldsymbol{X}\}(\boldsymbol{r}) - \frac{4\pi - \Omega_u}{4\pi}\hat{n}_u \times \mathcal{I}\{\boldsymbol{X}\}(\boldsymbol{r}) \qquad (1.22)$$

$$\mathcal{K}_u^{PV}\{\boldsymbol{X}\}(\boldsymbol{r}) = \int_{PV,S_u} d\boldsymbol{r}' \boldsymbol{X}(\boldsymbol{r}') \times \nabla' g_u(\boldsymbol{r}, \boldsymbol{r}'), \qquad (1.23)$$

where Ω_u is the internal solid angle. Inserting (1.22) in (1.21) and rearranging the terms, we have

$$-\hat{n}_u \times \boldsymbol{E}_u^i(\boldsymbol{r}) = \hat{n}_u \times \eta_u \mathcal{L}_u\{\boldsymbol{J}_u\}(\boldsymbol{r}) - \hat{n}_u \times \mathcal{K}_u^{PV}\{\boldsymbol{M}_u\}(\boldsymbol{r}) + \frac{\Omega_u}{4\pi}\boldsymbol{M}_u(\boldsymbol{r}). \quad (1.24)$$

Equation (1.24) is known as the normal electric-field IE (N-EFIE). Taking the cross product of both sides of (1.24) with $-\hat{n}_u$, T-EFIE can be obtained as

$$\begin{aligned}\hat{n}_u \times \hat{n}_u \times \boldsymbol{E}_u^i(\boldsymbol{r}) &= -\hat{n}_u \times \hat{n}_u \times \eta_u \mathcal{L}_u\{\boldsymbol{J}_u\}(\boldsymbol{r}) \\ &\quad + \hat{n}_u \times \hat{n}_u \times \mathcal{K}_u^{PV}\{\boldsymbol{M}_u\}(\boldsymbol{r}) - \frac{\Omega_u}{4\pi}\hat{n}_u \times \boldsymbol{M}_u(\boldsymbol{r}).\end{aligned} \qquad (1.25)$$

Following the same procedure for the magnetic field, N-MFIE and T-MFIE can be obtained as

$$\begin{aligned}-\hat{n}_u \times \boldsymbol{H}_u^i(\boldsymbol{r}) &= \hat{n}_u \times \eta_u^{-1} \mathcal{L}_u\{\boldsymbol{M}_u\}(\boldsymbol{r}) \\ &\quad + \hat{n}_u \times \mathcal{K}_u^{PV}\{\boldsymbol{J}_u\}(\boldsymbol{r}) - \frac{\Omega_u}{4\pi}\boldsymbol{J}_u(\boldsymbol{r})\end{aligned} \qquad (1.26)$$

$$\begin{aligned}\hat{n}_u \times \hat{n}_u \times \boldsymbol{H}_u^i(\boldsymbol{r}) &= -\hat{n}_u \times \hat{n}_u \times \eta_u^{-1} \mathcal{L}_u\{\boldsymbol{M}_u\}(\boldsymbol{r}) \\ &\quad - \hat{n}_u \times \hat{n}_u \times \mathcal{K}_u^{PV}\{\boldsymbol{J}_u\}(\boldsymbol{r}) + \frac{\Omega_u}{4\pi}\hat{n}_u \times \boldsymbol{J}_u(\boldsymbol{r}).\end{aligned} \qquad (1.27)$$

For the case of a PEC scatterer, the tangential component of the electric field disappears on the surface, hence, the magnetic equivalent current becomes zero. As commonly practiced for PEC problems, the combined-field IE (CFIE) can be derived by linearly adding T-EFIE and N-MFIE as

$$\begin{aligned}\alpha\hat{n}_u \times \hat{n}_u \times \eta_u^{-1}\boldsymbol{E}_u^i(\boldsymbol{r}) - (1-\alpha)\left[\hat{n}_u \times \boldsymbol{H}_u^i(\boldsymbol{r})\right] = \\ -\alpha\hat{n}_u \times \hat{n}_u \times \mathcal{L}_u\{\boldsymbol{J}_u\}(\boldsymbol{r}) + (1-\alpha)\left[\hat{n}_u \times \mathcal{K}_u^{PV}\{\boldsymbol{J}_u\}(\boldsymbol{r}) - \frac{\Omega_u}{4\pi}\boldsymbol{J}_u(\boldsymbol{r})\right].\end{aligned} \qquad (1.28)$$

In the case of homogeneous dielectric scatterers, a general formulation can be written as the combination of tangential/normal EFIE and MFIE formulations as

$$\sum_{u=1}^{U} \left[\begin{array}{c} a_u \text{T-EFIE}(u) + c_u \text{N-MFIE}(u) \\ b_u \text{T-MFIE}(u) + d_u \text{N-EFIE}(u) \end{array} \right], \tag{1.29}$$

where U is number of homogeneous media including the background medium.

1.3 Method of Moments (MoM)

All the integro-differential operators defined in the previous sections are linear operators. In order to solve SIEs, we consider a general form of IEs as

$$\mathscr{L}\{\boldsymbol{f}\}(\boldsymbol{r}) = \boldsymbol{g}(\boldsymbol{r}), \tag{1.30}$$

where $\mathscr{L}$ is a linear operator, $\boldsymbol{f}(\boldsymbol{r})$ is the unknown vector function, and $\boldsymbol{g}(\boldsymbol{r})$ is the known vector function. The unknown function $\boldsymbol{f}(\boldsymbol{r})$ is expanded in a series of known spatial basis functions $\boldsymbol{b}_n(\boldsymbol{r})$ as

$$\boldsymbol{f}(\boldsymbol{r}) \approx \sum_{n=1}^{N} \boldsymbol{a}_n \boldsymbol{b}_n(\boldsymbol{r}). \tag{1.31}$$

Substituting (1.31) in (1.30) we obtain

$$\sum_{n=1}^{N} \boldsymbol{a}_n \mathscr{L}\{\boldsymbol{b}_n\}(\boldsymbol{r}) = \boldsymbol{g}(\boldsymbol{r}). \tag{1.32}$$

Equation (1.32) has N unknowns. In order to get a sufficient number of equations, we test (1.32) with N different test functions $\boldsymbol{t}_m(\boldsymbol{r})$ for $m = 1, 2, ..., N$, leading to

$$\int d\boldsymbol{r} \boldsymbol{t}_m(\boldsymbol{r}) \cdot \sum_{n=1}^{N} \boldsymbol{a}_n \mathscr{L}\{\boldsymbol{b}_n\}(\boldsymbol{r}) = \int d\boldsymbol{r} \boldsymbol{t}_m(\boldsymbol{r}) \cdot \boldsymbol{g}(\boldsymbol{r}) \quad (m = 1, 2, ..., N). \tag{1.33}$$

Changing the order of integration and summation, the final matrix equation can be written as

$$\sum_{n=1}^{N} \boldsymbol{a}_n \bar{\boldsymbol{Z}}[m,n] = \boldsymbol{w}[m] \quad (m = 1, 2, ..., N), \tag{1.34}$$

where

$$\bar{\boldsymbol{Z}}[m,n] = \int d\boldsymbol{r} \boldsymbol{t}_m(\boldsymbol{r}) \cdot \mathscr{L}\{\boldsymbol{b}_n\}(\boldsymbol{r}) \tag{1.35}$$

$$\boldsymbol{w}[m] = \int d\boldsymbol{r} \boldsymbol{t}_m(\boldsymbol{r}) \cdot \boldsymbol{g}(\boldsymbol{r}). \tag{1.36}$$
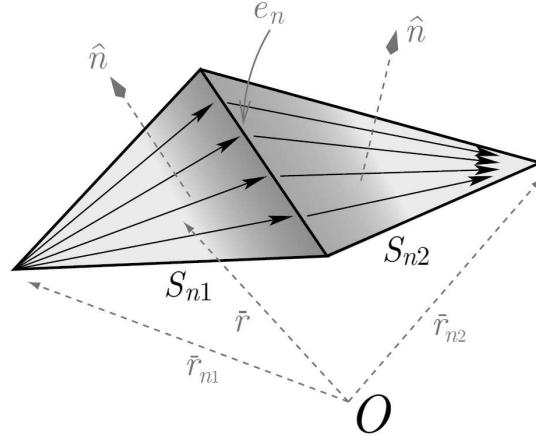
Figure 1.2: An RWG function defined on a pair of triangles sharing an edge [1].

A common discretization technique used in SIEs is triangularization. Using Galerkin method, Rao-Wilton-Glisson (RWG) functions can be used as basis and testing functions. They can be expressed as (see Figure 1.2)

$$
\boldsymbol{b}_n^{\text{RWG}}(\boldsymbol{r}) = \begin{cases} \dfrac{l_n}{2A_{n1}}(\boldsymbol{r} - \boldsymbol{r}_{n1}), & \boldsymbol{r} \in S_{n1} \\ \dfrac{l_n}{2A_{n2}}(\boldsymbol{r}_{n2} - \boldsymbol{r}), & \boldsymbol{r} \in S_{n2} \\ 0, & \boldsymbol{r} \notin S_n, \end{cases} \tag{1.37}
$$

where l_n represents the length of the common edge, and A_{n1} and A_{n2} are the areas of the first (S_{n1}) and the second (S_{n2}) triangles, respectively. The RWG functions are divergence conforming and their divergence is finite everywhere. They also satisfy charge neutrality, which means that the total charge introduced by each RWG function is zero. This can be verified by considering their divergences as

$$
\nabla \cdot \boldsymbol{b}_n^{\text{RWG}}(\boldsymbol{r}) = \begin{cases} \dfrac{l_n}{A_{n1}}, & \boldsymbol{r} \in S_{n1} \\ -\dfrac{l_n}{A_{n2}}, & \boldsymbol{r} \in S_{n2} \\ 0, & \boldsymbol{r} \notin S_n. \end{cases} \tag{1.38}
$$

Using the RWG functions, operators (1.16) to (1.18) can be discretized as

$$\bar{\boldsymbol{L}}^T[m,n] = ik \int_{S_m} d\boldsymbol{r} \boldsymbol{t}_m(\boldsymbol{r}) \cdot \int_{S_n} d\boldsymbol{r}' g(\boldsymbol{r},\boldsymbol{r}') \boldsymbol{b}_n(\boldsymbol{r}')$$
$$+ \frac{i}{k} \int_{S_m} d\boldsymbol{r} \boldsymbol{t}_m(\boldsymbol{r}) \cdot \int_{S_n} d\boldsymbol{r}' \nabla g(\boldsymbol{r},\boldsymbol{r}') \nabla' \cdot \boldsymbol{b}_n(\boldsymbol{r}') \tag{1.39}$$

$$\bar{\boldsymbol{L}}^N[m,n] = ik \int_{S_m} d\boldsymbol{r} \boldsymbol{t}_m(\boldsymbol{r}) \cdot \hat{\boldsymbol{n}} \times \int_{S_n} d\boldsymbol{r}' g(\boldsymbol{r},\boldsymbol{r}') \boldsymbol{b}_n(\boldsymbol{r}')$$
$$+ \frac{i}{k} \int_{S_m} d\boldsymbol{r} \boldsymbol{t}_m(\boldsymbol{r}) \cdot \hat{\boldsymbol{n}} \times \int_{S_n} d\boldsymbol{r}' \nabla g(\boldsymbol{r},\boldsymbol{r}') \nabla' \cdot \boldsymbol{b}_n(\boldsymbol{r}') \tag{1.40}$$

$$\bar{\boldsymbol{K}}^T[m,n] = \int_{S_m} d\boldsymbol{r} \boldsymbol{t}_m(\boldsymbol{r}) \cdot \int_{S_n} d\boldsymbol{r}' \boldsymbol{b}_n(\boldsymbol{r}') \times \nabla' g(\boldsymbol{r},\boldsymbol{r}') \tag{1.41}$$

$$\bar{\boldsymbol{K}}^N[m,n] = \int_{S_m} d\boldsymbol{r} \boldsymbol{t}_m(\boldsymbol{r}) \cdot \hat{\boldsymbol{n}} \times \int_{S_n} d\boldsymbol{r}' \boldsymbol{b}_n(\boldsymbol{r}') \times \nabla' g(\boldsymbol{r},\boldsymbol{r}') \tag{1.42}$$

$$\bar{\boldsymbol{I}}^T[m,n] = \int_{S_m} d\boldsymbol{r} \boldsymbol{t}_m(\boldsymbol{r}) \cdot \boldsymbol{b}_n(\boldsymbol{r}) \tag{1.43}$$

$$\bar{\boldsymbol{I}}^N[m,n] = \int_{S_m} d\boldsymbol{r} \boldsymbol{t}_m(\boldsymbol{r}) \cdot \hat{\boldsymbol{n}} \times \boldsymbol{b}_n(\boldsymbol{r}). \tag{1.44}$$

Considering the interaction between two half-RWG functions $\boldsymbol{t}_{ma}^{\text{RWG}}$ and $\boldsymbol{b}_{nb}^{\text{RWG}}$ associated with the ath triangle of the mth edge and the bth triangle of the nth edge, respectively, one can obtain

$$\bar{\boldsymbol{L}}^T[m,n,a,b] = ik\mathcal{A}_{ma,nb} \int_{S_{ma}} d\boldsymbol{r}(\boldsymbol{r} - \boldsymbol{r}_{ma}) \cdot \int_{S_{nb}} d\boldsymbol{r}'(\boldsymbol{r}' - \boldsymbol{r}_{nb}) g(\boldsymbol{r},\boldsymbol{r}')$$
$$- \frac{4i}{k}\mathcal{A}_{ma,nb} \int_{S_{ma}} d\boldsymbol{r} \int_{S_{nb}} d\boldsymbol{r}' g(\boldsymbol{r},\boldsymbol{r}') \tag{1.45}$$

$$\bar{\boldsymbol{L}}^N[m,n,a,b] = ik\mathcal{A}_{ma,nb} \int_{S_{ma}} d\boldsymbol{r} \left[(\boldsymbol{r} - \boldsymbol{r}_{ma}) \times \hat{\boldsymbol{n}}\right] \cdot \int_{S_{nb}} d\boldsymbol{r}'(\boldsymbol{r}' - \boldsymbol{r}_{nb}) g(\boldsymbol{r},\boldsymbol{r}')$$
$$- \frac{2i}{k}\mathcal{A}_{ma,nb} \int_{S_{ma}} d\boldsymbol{r} \left[(\boldsymbol{r} - \boldsymbol{r}_{ma}) \times \hat{\boldsymbol{n}}\right] \cdot \int_{S_{nb}} d\boldsymbol{r}' \nabla' g(\boldsymbol{r},\boldsymbol{r}') \tag{1.46}$$

$$\bar{\boldsymbol{K}}^T[m,n,a,b] = \mathcal{A}_{ma,nb} \int_{S_{ma}} d\boldsymbol{r}(\boldsymbol{r} - \boldsymbol{r}_{ma}) \cdot \left[(\boldsymbol{r} - \boldsymbol{r}_{nb}) \times \int_{S_{nb}} d\boldsymbol{r}' \nabla' g(\boldsymbol{r},\boldsymbol{r}')\right] \tag{1.47}$$

$$\bar{\boldsymbol{K}}^N[m,n,a,b] = \mathcal{A}_{ma,nb} \int_{S_{ma}} d\boldsymbol{r} \left[(\boldsymbol{r} - \boldsymbol{r}_{ma}) \times \hat{\boldsymbol{n}}\right] \cdot \left[(\boldsymbol{r} - \boldsymbol{r}_{nb}) \times \int_{S_{nb}} d\boldsymbol{r}' \nabla' g(\boldsymbol{r},\boldsymbol{r}')\right] \tag{1.48}$$

$$\bar{\boldsymbol{I}}^T[m,n,a,b] = \mathcal{A}_{ma,nb}\delta_{ma,nb} \int_{S_{ma}} d\boldsymbol{r}(\boldsymbol{r} - \boldsymbol{r}_{ma}) \cdot (\boldsymbol{r} - \boldsymbol{r}_{nb}) \tag{1.49}$$

$$\bar{\boldsymbol{I}}^N[m,n,a,b] = \mathcal{A}_{ma,nb}\delta_{ma,nb} \int_{S_{ma}} d\boldsymbol{r}(\boldsymbol{r} - \boldsymbol{r}_{ma}) \cdot \hat{\boldsymbol{n}} \times (\boldsymbol{r} - \boldsymbol{r}_{nb}), \tag{1.50}$$

9

where

$$\delta_{ma,nb} = \begin{cases} 1, & m = n \text{ and } a = b \\ \\ 0, & \text{otherwise,} \end{cases} \tag{1.51}$$

$$\mathcal{A}_{ma,nb} = \frac{l_m l_n}{4 A_{ma} A_{nb}} \gamma_{ma} \gamma_{nb}, \tag{1.52}$$

and $\gamma_{nb}, \gamma_{ma} = \pm 1$, depending on the direction of the basis and testing functions on triangles.

CHAPTER 2

EQUIVALENCE PRINCIPLE ALGORITHM

2.1　General Idea of EPA

In EPA, the problem domain is divided into subdomains and each subdomain is enclosed by an ES. The general idea of EPA is to transform the original unknowns in each subdomain to new unknowns on the surrounding ES by employing Huygens' principle. The solution of each subdomain is considered by relating the scattered equivalent sources on the ES to the incident equivalent sources on the same ES via scattering operators, while the electromagnetic interactions between subdomains are calculated via translation operators. The favorable properties of EPA can be summarized as follows.

1. Fewer unknowns: While the original scatterer can have fine meshes due to fine geometrical details, the corresponding ES can be chosen as a smooth one. In addition, the equivalent sources on the ES usually have smoother distributions than the actual currents on the original scatterer. As a result, the final number of the unknowns can be considerably small in comparison to the original problem.

2. Efficient: Whenever there are identical subdomains, equivalence principle and translation operators can be reused without recalculating them, making the algorithm more efficient in solving periodic and array structures.

3. Rigorous: In each subdomain, the electromagnetic interactions are calculated directly. In addition, between different subdomains, all interactions are computed rigorously using surface integral operators. Hence, EPA does not change the full-wave nature of the underlying formulation.

4. Well-conditioned: Using EPA, created matrix equations are always better conditioned than those obtained from the direct applications of MoM. This is because the electromagnetic interactions are re-organized such that self interactions of equivalence problems turn into identity operators.

2.2 EPA for a Single-Domain Problem

In this section, for simplicity, we consider a single-domain scattering problem. The first step of the algorithm is to define incident equivalent current densities on the ES. Using the equivalence principle given in Chapter 1, they can be written as

$$\boldsymbol{J}^{\text{i}}(\boldsymbol{r}) = \hat{\boldsymbol{n}} \times \boldsymbol{H}^{\text{i}}(\boldsymbol{r}) \tag{2.1}$$

$$\boldsymbol{M}^{\text{i}}(\boldsymbol{r}) = -\hat{\boldsymbol{n}} \times \boldsymbol{E}^{\text{i}}(\boldsymbol{r}), \tag{2.2}$$

where $\hat{\boldsymbol{n}}$ is outward unit normal of the ES. After this step, the solution can be divided into three steps that can be represented by three operators as follows.

1. Outside-In (OI) Propagation Operator ($\mathcal{A}$): This operator takes incident equivalent currents and creates incident electric and magnetic fields on the surface of the original scatterer by radiating them using the operators defined in (1.16) to (1.18).

2. Current Solver ($\mathcal{B}$): Since the above step provides the incident fields on the surface of original scatterer, by employing a proper SIE solver, such as given in (1.28) for PEC objects and (1.29) for penetrable objects, the induced or equivalent (actual) currents on the surface of the original scatterer can be calculated.

3. Inside-Out (IO) Propagation Operator ($\mathcal{C}$): This operator gives the scattered equivalent current densities on the ES by radiating the actual currents on the scatterer.

The overall procedure is illustrated in Figure 2.1, and it can be written in a matrix form as

$$\begin{bmatrix} \boldsymbol{J}^{\text{s}} \\ \boldsymbol{M}^{\text{s}} \end{bmatrix} = \mathcal{S} \begin{bmatrix} \boldsymbol{J}^{\text{i}} \\ \boldsymbol{M}^{\text{i}} \end{bmatrix}, \tag{2.3}$$

12

where $\boldsymbol{J}^s/\boldsymbol{M}^s$ and $\boldsymbol{J}^i/\boldsymbol{M}^i$ are scattered and incident equivalent currents and

$$\boldsymbol{\mathcal{S}} = \boldsymbol{\mathcal{C}}(\boldsymbol{\mathcal{B}})^{-1}\boldsymbol{\mathcal{A}}. \tag{2.4}$$

Here $\boldsymbol{\mathcal{S}}$ is called the scattering operator that represents the direct scattering of incident fields from the scatterer located in the ES. Since the scattering operator depends on the SIE solver, we define its matrix form for PEC and penetrable objects as follows.

2.2.1 Scattering Operator for PEC Scatterers

Assuming a PEC scatterer, we consider CFIE in (1.28). The operators in (2.4) can be expressed in terms of operators defined in (1.16) to (1.18). Considering the right-hand side of (1.28) and using (1.14) and (1.15), OI propagation operator can be written as

$$\boldsymbol{\mathcal{A}} = \left[\alpha\boldsymbol{\mathcal{L}}_{tan}^{OI} + (1-\alpha)\hat{\boldsymbol{n}} \times \boldsymbol{\mathcal{K}}^{OI} \quad -\frac{\alpha}{\eta_0}\boldsymbol{\mathcal{K}}_{tan}^{OI} + \frac{(1-\alpha)}{\eta_0}\hat{\boldsymbol{n}} \times \boldsymbol{\mathcal{L}}^{OI} \right], \tag{2.5}$$

where $\boldsymbol{X}_{tan}$ is $-\hat{\boldsymbol{n}} \times \hat{\boldsymbol{n}} \times \boldsymbol{X}$. This operator creates the desired incident fields on the surface of the PEC object, and it involves source points on the ES and observation points on the PEC scatterer. Considering the left-hand side of (1.28), the current solver can be written as

$$\boldsymbol{\mathcal{B}} = \left[\alpha\boldsymbol{\mathcal{L}}_{tan} + (1-\alpha)\left(\hat{\boldsymbol{n}} \times \boldsymbol{\mathcal{K}} - \frac{1}{2}\boldsymbol{\mathcal{I}}\right) \right]. \tag{2.6}$$

In this operator, a direct inversion of the corresponding matrix is required that is considered to be one of main limitations of EPA. In the current solution, both source and observation points are on the surface of the PEC object. Finally, by employing the equivalence principle, the IO propagation operator can be expressed as

$$\boldsymbol{\mathcal{C}} = \left[\begin{array}{c} \hat{\boldsymbol{n}}_{ES} \times \boldsymbol{\mathcal{K}}^{IO} \\ -\eta_0\hat{\boldsymbol{n}}_{ES} \times \boldsymbol{\mathcal{L}}^{IO} \end{array} \right], \tag{2.7}$$

where $\hat{\boldsymbol{n}}_{ES}$ represents outward unit normal of the ES. Here, the source and observation points are on the surface of the PEC object and the ES, respectively. Since the scatterer is a PEC, there is no magnetic current density on its surface and the output of the current solver is only the electric current density $\boldsymbol{J}_{obj}^s$. The IO propagation operator transforms $\boldsymbol{J}_{obj}^s$ to $\boldsymbol{J}^s$ and $\boldsymbol{M}^s$ by projecting the scattered fields on the ES.
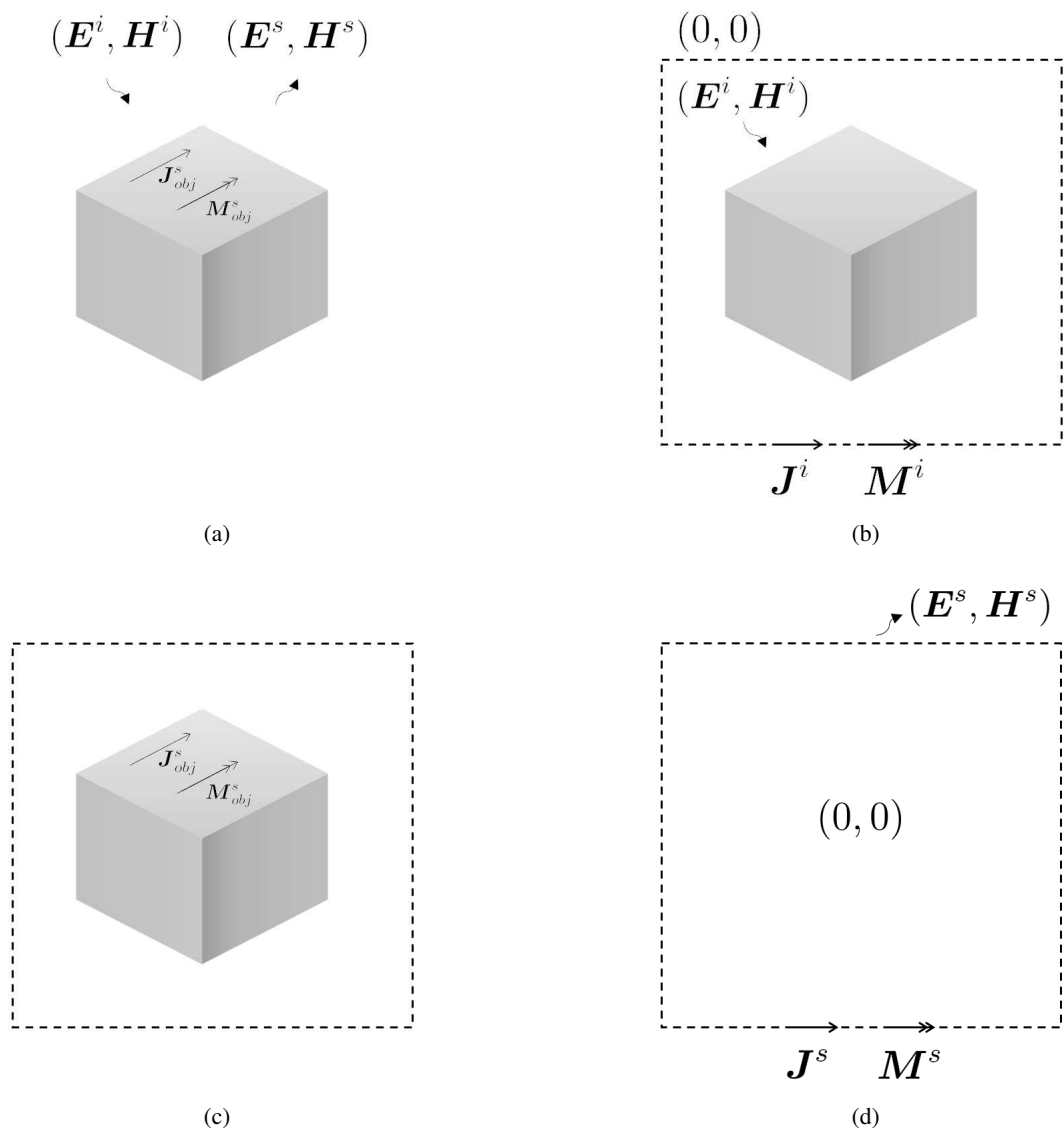
Figure 2.1: EPA procedure for solving a single-domain problem: (a) Original problem, (b) OI propagation, (c) current solution, (d) IO propagation.

2.2.2 Scattering Operator for Penetrable Scatterers

In the case of a penetrable scatterer, we consider the general combination of the tangential/normal EFIE and MFIE formulations given in (1.29). Following a similar procedure, the operators in (2.4) can be expressed as

$$
\mathcal{A} = \begin{bmatrix} a_0 \mathcal{L}_{tan}^{OI} + b_0 \hat{\boldsymbol{n}} \times \mathcal{K}^{OI} & -a_0/\eta_0 \mathcal{K}_{tan}^{OI} + b_0/\eta_0 \hat{\boldsymbol{n}} \times \mathcal{L}^{OI} \\ d_0 \eta_0 \mathcal{K}_{tan}^{OI} - c_0 \eta_0 \hat{\boldsymbol{n}} \times \mathcal{L}^{OI} & d_0 \mathcal{L}_{tan}^{OI} + c_0 \hat{\boldsymbol{n}} \times \mathcal{K}^{OI} \end{bmatrix}, \qquad (2.8)
$$

$$
\mathcal{B} = \begin{bmatrix} \mathcal{B}^{11} & \mathcal{B}^{12} \\ \mathcal{B}^{21} & \mathcal{B}^{22} \end{bmatrix}, \qquad (2.9)
$$

and

$$
\mathcal{C} = \begin{bmatrix} \hat{\boldsymbol{n}}_{ES} \times \mathcal{K}^{IO} & 1/\eta_0 \hat{\boldsymbol{n}}_{ES} \times \mathcal{L}^{IO} \\ -\eta_0 \hat{\boldsymbol{n}}_{ES} \times \mathcal{L}^{IO} & \hat{\boldsymbol{n}}_{ES} \times \mathcal{K}^{IO} \end{bmatrix}. \qquad (2.10)
$$

In the above, we have

$$
\mathcal{B}^{11} = (a_0 \mathcal{L}_0 + a_p \mathcal{L}_p)_{tan} + \hat{\boldsymbol{n}} \times (b_0 \mathcal{K}_0 - b_p \mathcal{K}_p) - \frac{1}{2}(b_0 + b_p)\mathcal{I} \qquad (2.11)
$$

$$
\begin{aligned}
\mathcal{B}^{12} = & \hat{\boldsymbol{n}} \times \left(\frac{b_0}{\eta_0} \mathcal{L}_0 - \frac{b_p}{\eta_p} \mathcal{L}_p \right) - \left(\frac{a_0}{\eta_0} \mathcal{K}_0 + \frac{a_p}{\eta_p} \mathcal{K}_p \right)_{tan} \\
& - \frac{1}{2} \left(\frac{a_0}{\eta_0} - \frac{a_p}{\eta_p} \right) \hat{\boldsymbol{n}} \times \mathcal{I}
\end{aligned} \qquad (2.12)
$$

$$
\begin{aligned}
\mathcal{B}^{21} = & \hat{\boldsymbol{n}} \times (-c_0 \eta_0 \mathcal{L}_0 + c_p \eta_p \mathcal{L}_p) + (d_0 \eta_0 \mathcal{K}_0 + d_p \eta_p \mathcal{K}_p)_{tan} \\
& - \frac{1}{2}(\eta_0 d_0 - \eta_p d_p)\hat{\boldsymbol{n}} \times \mathcal{I}
\end{aligned} \qquad (2.13)
$$

$$
\mathcal{B}^{22} = (d_0 \mathcal{L}_0 + d_p \mathcal{L}_p)_{tan} + \hat{\boldsymbol{n}} \times (c_0 \mathcal{K}_0 - c_p \mathcal{K}_p) - \frac{1}{2}(c_0 + c_p)\mathcal{I}. \qquad (2.14)
$$

We further note that the arrangements of the source and observation points are same as those in the PEC case. In addition, $\hat{\boldsymbol{n}}$ is the outward unit normal of the scatterer, while the indices 0 and p indicate the material parameters and the corresponding Green's functions used in the operators $\mathcal{L}$ and $\mathcal{K}$.
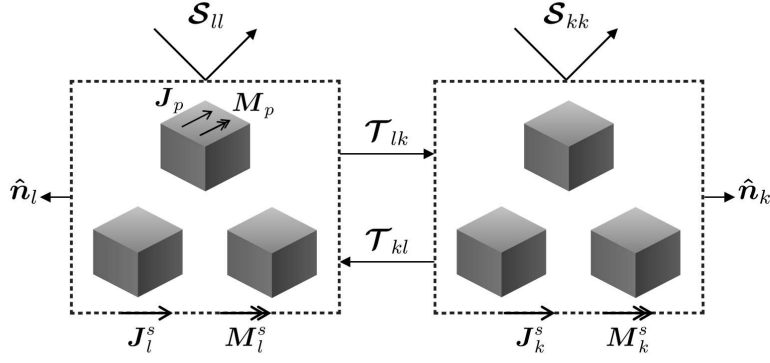
Figure 2.2: An illustration of EPA operators for subdomains l and k. In the figure, $\boldsymbol{J}_p$ and $\boldsymbol{M}_p$ are the equivalent current densities on the surface of the pth original scatterer. In addition, $\{\boldsymbol{J}_l^{\text{s}}, \boldsymbol{M}_l^{\text{s}}\}$ and $\{\boldsymbol{J}_k^{\text{s}}, \boldsymbol{M}_k^{\text{s}}\}$ represent scattered currents densities on the lth ES and the kth ES, respectively, while $\{\boldsymbol{\mathcal{S}}_{ll}, \boldsymbol{\mathcal{S}}_{kk}\}$ and $\{\boldsymbol{\mathcal{T}}_{lk}, \boldsymbol{\mathcal{T}}_{kl}\}$ are scattering and translation operators.

2.3 EPA for a Multi-Domain Problem

Now, we consider P separate scatterers represented by $\{D_1, D_2, ..., D_P\}$ located in a homogeneous background D_0. These scatterers are grouped into L groups. Each group is enclosed by an ES and it can include one or multiple scatterers. However, an ES cannot touch other ESs or the scatterers it encloses. The direct scattering of incident fields in each subdomain can be calculated via a scattering operator $\boldsymbol{\mathcal{S}}$ as described earlier, while the interactions between subdomains are taken into account using translation operators $\boldsymbol{\mathcal{T}}$. For calculating the scattered equivalent currents on the lth ES, the fields created by the scattered currents on the other ESs are projected on it via translation operators and the created equivalent currents are considered as new incident currents. Such an interaction between two subdomains are illustrated in Figure 2.2. Employing translation operators, (2.3) can be expressed for a general case as

$$\begin{bmatrix} \boldsymbol{J}_l^{\text{s}} \\ \boldsymbol{M}_l^{\text{s}} \end{bmatrix} = \boldsymbol{\mathcal{S}}_{ll} \begin{bmatrix} \boldsymbol{J}_l^{\text{i}} \\ \boldsymbol{M}_l^{\text{i}} \end{bmatrix} + \boldsymbol{\mathcal{S}}_{ll} \left(\sum_{k=1, k \neq l}^{L} \boldsymbol{\mathcal{T}}_{lk} \begin{bmatrix} \boldsymbol{J}_k^{\text{s}} \\ \boldsymbol{M}_k^{\text{s}} \end{bmatrix} \right), \qquad (2.15)$$

where a translation operator $\mathcal{T}_{lk}$ is defined as

$$\mathcal{T}_{lk} = \begin{bmatrix} \hat{n}_l \times \mathcal{K}_{lk} & 1/\eta_0 \hat{n}_l \times \mathcal{L}_{lk} \\ -\eta_0 \hat{n}_l \times \mathcal{L}_{lk} & \hat{n}_l \times \mathcal{K}_{lk} \end{bmatrix}. \tag{2.16}$$

In this expression, the observation and source points are located on the surfaces indicated by the first and the second indices, respectively. Since the translation operators are applied on the scattered equivalent currents, they have the same expression for PEC and penetrable scatterers.

2.4 Matrix Representation of EPA

By writing (2.15) for scattered equivalent currents on all ESs, the matrix equation for EPA can be derived as

$$\begin{bmatrix} \mathcal{I} & -\mathcal{S}_{11}\mathcal{T}_{12} & \cdots & -\mathcal{S}_{11}\mathcal{T}_{1L} \\ -\mathcal{S}_{22}\mathcal{T}_{21} & \mathcal{I} & \cdots & -\mathcal{S}_{22}\mathcal{T}_{2L} \\ \vdots & \vdots & \ddots & \vdots \\ -\mathcal{S}_{LL}\mathcal{T}_{L1} & -\mathcal{S}_{LL}\mathcal{T}_{L2} & \cdots & \mathcal{I} \end{bmatrix} \cdot \begin{bmatrix} C_1^s \\ C_2^s \\ \vdots \\ C_L^s \end{bmatrix} = \begin{bmatrix} \mathcal{S}_{11}C_1^i \\ \mathcal{S}_{22}C_2^i \\ \vdots \\ \mathcal{S}_{LL}C_L^i \end{bmatrix}, \tag{2.17}$$

where

$$C_l^s = \begin{bmatrix} J_l^s \\ M_l^s \end{bmatrix} = \begin{bmatrix} \hat{n}_l \times H^s \\ -\hat{n}_l \times E^s \end{bmatrix} \tag{2.18}$$

represents the scattered equivalent current densities, and

$$C_l^i = \begin{bmatrix} J_l^i \\ M_l^i \end{bmatrix} = \begin{bmatrix} \hat{n}_l \times H^i \\ -\hat{n}_l \times E^i \end{bmatrix} \tag{2.19}$$

represents the incident equivalent current densities on the lth ES. By solving (2.17) for scattered currents, scattered fields outside all ESs can be found by using (1.14) and (1.15). Unlike MoM formulations for PEC and penetrable objects, EPA has identity operators in diagonal blocks of the main matrix, leading to a relatively sparse equation. Moreover, it will be shown in the next section that identity operators can be replaced with identity matrices during the construction of a matrix equation. This further enhances the conditioning and leads to fast iterative convergence. It is remarkable that the convergence of an iterative solution using EPA is almost independent of the underlying SIE formulation used in the scattering operators.

17

2.5 Electromagnetic Excitation

In the numerical implementation of EPA considered in this thesis, the following excitations are employed.

- Plane wave

- Hertzian dipole

- Delta gap

For a plane wave, incident electric and magnetic fields can be written as

$$\boldsymbol{E}^{\mathrm{i}}(\boldsymbol{r}) = \hat{\boldsymbol{e}} E_a \exp(ik\hat{\boldsymbol{k}} \cdot \boldsymbol{r}) \tag{2.20}$$

$$\boldsymbol{H}^{\mathrm{i}}(\boldsymbol{r}) = \frac{1}{\eta}\hat{\boldsymbol{k}} \times \boldsymbol{E}^{\mathrm{i}}(\boldsymbol{r}) = \hat{\boldsymbol{k}} \times \hat{\boldsymbol{e}}\frac{E_a}{\eta} \exp(ik\hat{\boldsymbol{k}} \cdot \boldsymbol{r}), \tag{2.21}$$

where $\hat{\boldsymbol{e}}$ is the electric field polarization, $\hat{\boldsymbol{k}}$ is the propagation direction that is perpendicular to $\hat{\boldsymbol{e}}$, E_a is the electric field amplitude, and k is the wavenumber. On the other hand, electric and magnetic fields created by a Hertzian dipole with dipole moment $\boldsymbol{I}_D$ located at $\boldsymbol{r}_D$ can be derived as

$$\begin{aligned}
\boldsymbol{E}^{\mathrm{i}}(\boldsymbol{r}) = i\omega\mu\frac{\exp(ikR)}{4\pi R}\Bigg\{ &\boldsymbol{I}_D\left(1 + \frac{i}{kR} - \frac{1}{k^2R^2}\right) \\
&- \boldsymbol{I}_D \cdot \hat{\boldsymbol{R}}\hat{\boldsymbol{R}}\left(1 + \frac{3i}{kR} - \frac{3}{k^2R^2}\right)\Bigg\}
\end{aligned} \tag{2.22}$$

$$\boldsymbol{H}^{\mathrm{i}}(\boldsymbol{r}) = \boldsymbol{I}_D \times \hat{\boldsymbol{R}}\frac{\exp(ikR)}{4\pi R}\left(\frac{1}{R} - ik\right), \tag{2.23}$$

where $\boldsymbol{R} = R\hat{\boldsymbol{R}} = \boldsymbol{r} - \boldsymbol{r}_D$. Unlike plane-wave and Hertzian dipole excitations, which are completely external without a physical connection to objects, it is possible to define local excitations, such as delta-gap excitations. A delta-gap can be considered as a voltage source placed on an infinitely narrow opening between two triangles of the discretization. The electric field created by such a voltage source can be defined as (see Figure 2.3)

$$\boldsymbol{E}^{\mathrm{i}}(\boldsymbol{r}) = I \lim_{d\to 0} \frac{\hat{\boldsymbol{u}}\delta(\boldsymbol{r}, \boldsymbol{r}_e)}{d}, \tag{2.24}$$

where I is a complex value determining the strength of the feed, $\hat{\boldsymbol{u}}$ is the unit vector perpendicular to the edge in the plane of triangles, $\boldsymbol{r}_e$ is any point on the edges,

18
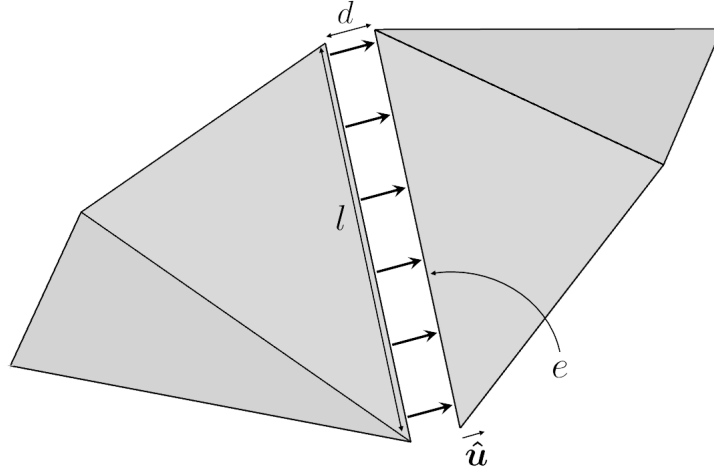
Figure 2.3: An illustration of a delta-gap source.

and d is the theoretical gap width. The gap will converge to edge e as $d \to 0$. As delta-gap sources are located on the objects without cross interactions, a practical way to use them in EPA is to keep them on the right-hand side of (2.17) instead of defining equivalent incident currents. This means that, we can replace the product of OI propagation operator and incident currents directly with the incident fields.

2.6   Discretization of EPA

In order to discretize equation (2.17), all operators are discretized by using the RWG functions defined in (1.37) as the basis and testing functions. We note that discretized operators are applied on fields and currents that have already been expanded with basis functions. We need to consider this while discretizing the right-hand side and the non-diagonal terms on the left-hand side of (2.17). For this purpose, $Gram$ matrices are employed [19].

In order to discretize the operators, the currents are expanded with the RWG functions as

$$\boldsymbol{J}_l^{\mathrm{s}}(\boldsymbol{r}) = \sum_{n=1}^{N_l} a_{n,J_l^{\mathrm{s}}} \boldsymbol{b}_n^{\mathrm{RWG}}(\boldsymbol{r}) \tag{2.25}$$

19

$$M_l^{\text{s}}(\boldsymbol{r}) = \sum_{n=1}^{N_l} a_{n,M_l^{\text{s}}} \boldsymbol{b}_n^{\text{RWG}}(\boldsymbol{r}) \tag{2.26}$$

$$J_l^{\text{i}}(\boldsymbol{r}) = \sum_{n=1}^{N_l} a_{n,J_l^{\text{i}}} \boldsymbol{b}_n^{\text{RWG}}(\boldsymbol{r}) \tag{2.27}$$

$$M_l^{\text{i}}(\boldsymbol{r}) = \sum_{n=1}^{N_l} a_{n,M_l^{\text{i}}} \boldsymbol{b}_n^{\text{RWG}}(\boldsymbol{r}), \tag{2.28}$$

where N_l is number of basis functions on the lth ES. For $\boldsymbol{\mathcal{S}}_{ll}$ to be applied on C_l^{i} on the right-hand side of (2.17), C_l^{i} needs to be expanded in terms of basis functions. This can be done by discretizing and solving an equation as

$$\begin{bmatrix} \boldsymbol{\mathcal{I}}_{ll} & 0 \\ 0 & \boldsymbol{\mathcal{I}}_{ll} \end{bmatrix} \cdot \begin{bmatrix} \boldsymbol{J}_l^{\text{i}} \\ \boldsymbol{M}_l^{\text{i}} \end{bmatrix} = \begin{bmatrix} \hat{\boldsymbol{n}}_l \times \boldsymbol{H}^{\text{i}} \\ -\hat{\boldsymbol{n}}_l \times \boldsymbol{E}^{\text{i}} \end{bmatrix}. \tag{2.29}$$

The solution can be written as

$$\boldsymbol{a}_l^{\text{i}} = \begin{bmatrix} \boldsymbol{a}_{J_l^{\text{i}}} \\ \boldsymbol{a}_{M_l^{\text{i}}} \end{bmatrix} = \bar{\boldsymbol{U}}_{ll}^{-1} \cdot \begin{bmatrix} \boldsymbol{v}_l^{H^{\text{i}},N} \\ -\boldsymbol{v}_l^{E^{\text{i}},N} \end{bmatrix}, \tag{2.30}$$

where

$$\bar{\boldsymbol{U}}_{ll} = \begin{bmatrix} \bar{\boldsymbol{I}}_{ll}^T & 0 \\ 0 & \bar{\boldsymbol{I}}_{ll}^T \end{bmatrix} \tag{2.31}$$

$$\boldsymbol{v}_l^{H^{\text{i}},N} = \int d\boldsymbol{r} \boldsymbol{t}_m(\boldsymbol{r}) \cdot \hat{\boldsymbol{n}}_l \times \boldsymbol{H}^{\text{i}} \tag{2.32}$$

$$\boldsymbol{v}_l^{E^{\text{i}},N} = \int d\boldsymbol{r} \boldsymbol{t}_m(\boldsymbol{r}) \cdot \hat{\boldsymbol{n}}_l \times \boldsymbol{E}^{\text{i}}. \tag{2.33}$$

In the above, $\bar{\boldsymbol{U}}_{ll}$ represents a sparse Gram matrix. Thus, the scattering operator $\boldsymbol{\mathcal{S}}_{ll}$ can be discretized as

$$\bar{\boldsymbol{S}}_{ll} = \bar{\boldsymbol{C}}_{lp} \cdot (\bar{\boldsymbol{B}}_{pp})^{-1} \cdot \bar{\boldsymbol{A}}_{pl}, \tag{2.34}$$

where

$$\bar{\boldsymbol{A}}_{pl} = \begin{bmatrix} \alpha_p \bar{\boldsymbol{L}}_{pl}^T + (1-\alpha_p) \bar{\boldsymbol{K}}_{pl}^N & -\alpha_p/\eta_0 \bar{\boldsymbol{K}}_{pl}^T + (1-\alpha_p)/\eta_0 \bar{\boldsymbol{L}}_{pl}^N \end{bmatrix} \tag{2.35}$$

$$\bar{\boldsymbol{B}}_{pp} = \begin{bmatrix} \alpha_p \bar{\boldsymbol{L}}_{pp}^T + (1-\alpha_p) \left(\bar{\boldsymbol{K}}_{pp}^N - \frac{1}{2} \bar{\boldsymbol{I}}_{pp}^T \right) \end{bmatrix} \tag{2.36}$$

$$\bar{\boldsymbol{C}}_{lp} = \begin{bmatrix} \bar{\boldsymbol{K}}_{lp}^N \\ -\eta_0 \bar{\boldsymbol{L}}_{lp}^N \end{bmatrix} \tag{2.37}$$

for a PEC scatterer case and

$$\bar{A}_{pl} = \begin{bmatrix} a_0 \bar{L}_{pl}^T + b_0 \bar{K}_{pl}^N & -a_0/\eta_0 \bar{K}_{pl}^T + b_0/\eta_0 \bar{L}_{pl}^N \\ d_0 \eta_0 \bar{K}_{pl}^T - c_0 \eta_0 \bar{L}_{pl}^N & d_0 \bar{L}_{pl}^T + c_0 \bar{K}_{pl}^N \end{bmatrix} \tag{2.38}$$

$$\bar{B}_{pp} = \begin{bmatrix} \bar{B}^{11} & \bar{B}^{12} \\ \bar{B}^{21} & \bar{B}^{22} \end{bmatrix} \tag{2.39}$$

$$\bar{C}_{lp} = \begin{bmatrix} \bar{K}_{lp}^N & 1/\eta_0 \bar{L}_{lp}^N \\ -\eta_0 \bar{L}_{lp}^N & \bar{K}_{lp}^N \end{bmatrix} \tag{2.40}$$

for a penetrable scatterer. In the above, we have

$$\bar{B}^{11} = a_0 \bar{L}_0^T + a_p \bar{L}_p^T + b_0 \bar{K}_0^N - b_p \bar{K}_p^N - \frac{1}{2}(b_0 + b_p)\bar{I}^T \tag{2.41}$$

$$\bar{B}^{12} = \frac{b_0}{\eta_0} \bar{L}_0^N - \frac{b_p}{\eta_p} \bar{L}_p^N - \frac{a_0}{\eta_0} \bar{K}_0^T + \frac{a_p}{\eta_p} \bar{K}_p^T - \frac{1}{2}\left(\frac{a_0}{\eta_0} - \frac{a_p}{\eta_p}\right)\bar{I}^N \tag{2.42}$$

$$\bar{B}^{21} = -c_0 \eta_0 \bar{L}_0^N + c_p \eta_p \bar{L}_p^N + d_0 \eta_0 \bar{K}_0^T + d_p \eta_p \bar{K}_p^T - \frac{1}{2}(\eta_0 d_0 - \eta_p d_p)\bar{I}^N \tag{2.43}$$

$$\bar{B}^{22} = d_0 \bar{L}_0^T + d_p \bar{L}_p^T + c_0 \bar{K}_0^N - c_p \bar{K}_p^N - \frac{1}{2}(c_0 + c_p)\bar{I}^T. \tag{2.44}$$

Similarly, the translation operator can be discretized as

$$\bar{T}_{lk} = \begin{bmatrix} \bar{K}_{lk}^N & 1/\eta_0 \bar{L}_{lk}^N \\ -\eta_0 \bar{L}_{lk}^N & \bar{K}_{lk}^N \end{bmatrix}. \tag{2.45}$$

Finally, (2.17) can be written in a discretized form as

$$\begin{bmatrix} \bar{Z}_{11} & \bar{Z}_{12} & \cdots & \bar{Z}_{1L} \\ \bar{Z}_{21} & \bar{Z}_{22} & \cdots & \bar{Z}_{21} \\ \vdots & \vdots & \ddots & \vdots \\ \bar{Z}_{L1} & \bar{Z}_{L2} & \cdots & \bar{Z}_{LL} \end{bmatrix} \cdot \begin{bmatrix} a_1^s \\ a_2^s \\ \vdots \\ a_L^s \end{bmatrix} = \begin{bmatrix} w_1^i \\ w_2^i \\ \vdots \\ w_L^i \end{bmatrix}, \tag{2.46}$$

where

$$\bar{Z}_{lk} = \begin{cases} \bar{U}_{ll}, & l = k \\ -\bar{S}_{ll} \cdot (\bar{U}_{ll})^{-1} \cdot \bar{T}_{lk}, & l \neq k \end{cases} \tag{2.47}$$

$$w_l^i = \bar{S}_{ll} \cdot \bar{U}_{ll}^{-1} \cdot C_l^i. \tag{2.48}$$

The conditioning of (2.46) can be enhanced by multiplying the whole equation from left-hand side with $\bar{U}_{ll}^{-1}$. Then (2.47) and (2.48) become

$$\bar{Z}_{lk} = \begin{cases} \boldsymbol{I}, & l = k \\ -\bar{\boldsymbol{U}}_{ll}^{-1} \cdot \bar{\boldsymbol{S}}_{ll} \cdot \bar{\boldsymbol{U}}_{ll}^{-1} \cdot \bar{\boldsymbol{T}}_{lk}, & l \neq k \end{cases} \tag{2.49}$$

$$\boldsymbol{w}_l^{\mathrm{i}} = \bar{\boldsymbol{U}}_{ll}^{-1} \cdot \bar{\boldsymbol{S}}_{ll} \cdot \bar{\boldsymbol{U}}_{ll}^{-1} \cdot \boldsymbol{C}_l^{\mathrm{i}}, \tag{2.50}$$

where $\boldsymbol{I}$ represents identity matrix. For array structures with identical elements, $\bar{\boldsymbol{U}}_{ll}^{-1} \cdot \bar{\boldsymbol{S}}_{ll} \cdot \bar{\boldsymbol{U}}_{ll}^{-1}$ is calculated once, which makes EPA a suitable method for analyzing array structures.

2.7 T-EPA

In (2.46), for expanding the projected fields on ESs, identity operator is used. However, identity operator is known to introduce inaccuracy when discretized with low-order functions [20]. This inaccuracy is the root of the inaccuracy of MFIE in comparison to EFIE using the RWG functions. In the context of EPA, an alternative way for calculating the projected fields accurately is using integro-differential operators [21, 22]. In this method, instead of solving (2.29), an equation in the form of

$$\begin{bmatrix} \eta_0 \boldsymbol{\mathcal{L}}_{tan} & -\boldsymbol{\mathcal{K}}_{tan}^{PV} \\ \boldsymbol{\mathcal{K}}_{tan}^{PV} & 1/\eta_0 \boldsymbol{\mathcal{L}}_{tan} \end{bmatrix} \cdot \begin{bmatrix} \boldsymbol{J}_l^{\mathrm{i}} \\ \boldsymbol{M}_l^{\mathrm{i}} \end{bmatrix} = -\frac{1}{2} \begin{bmatrix} \boldsymbol{E}_{tan}^{\mathrm{i}} \\ \boldsymbol{H}_{tan}^{\mathrm{i}} \end{bmatrix} \tag{2.51}$$

is used to expand equivalent currents that represents incident fields. In order to derive (2.51), we consider the equivalent current densities given in (2.1) and (2.2). According to the equivalence principle, these sources create zero fields outside of the ES, which means that the null equation

$$\begin{bmatrix} \eta_0 \boldsymbol{\mathcal{L}}_{tan} & -\boldsymbol{\mathcal{K}}_{tan} \\ \boldsymbol{\mathcal{K}}_{tan} & 1/\eta_0 \boldsymbol{\mathcal{L}}_{tan} \end{bmatrix} \cdot \begin{bmatrix} \hat{\boldsymbol{n}}_l \times \boldsymbol{H}^{\mathrm{i}} \\ -\hat{\boldsymbol{n}}_l \times \boldsymbol{E}^{\mathrm{i}} \end{bmatrix} = \begin{bmatrix} 0 \\ 0 \end{bmatrix} \tag{2.52}$$

holds. Replacing the $\boldsymbol{\mathcal{K}}$ operator with (1.22), we have

$$\begin{bmatrix} \eta_0 \boldsymbol{\mathcal{L}}_{tan} & -\boldsymbol{\mathcal{K}}_{tan}^{PV} + 1/2\hat{\boldsymbol{n}}_l \times \boldsymbol{\mathcal{I}} \\ \boldsymbol{\mathcal{K}}_{tan}^{PV} - 1/2\hat{\boldsymbol{n}}_l \times \boldsymbol{\mathcal{I}} & 1/\eta_0 \boldsymbol{\mathcal{L}}_{tan} \end{bmatrix} \cdot \begin{bmatrix} \hat{\boldsymbol{n}}_l \times \boldsymbol{H}^{\mathrm{i}} \\ -\hat{\boldsymbol{n}}_l \times \boldsymbol{E}^{\mathrm{i}} \end{bmatrix} = \begin{bmatrix} 0 \\ 0 \end{bmatrix}. \tag{2.53}$$

Then, by applying identity operators on the fields and moving them to the right-hand side of the equation, we can obtain (2.51). By considering the same projection method, IO and translation operators can be written as

$$\mathcal{C}_{lp} = \begin{bmatrix} \eta_0(\mathcal{L}_{lp})_{tan} & -(\mathcal{K}_{lp})_{tan} \\ (\mathcal{K}_{lp})_{tan} & 1/\eta_0(\mathcal{L}_{lp})_{tan} \end{bmatrix} \qquad (2.54)$$

$$\mathcal{T}_{lk} = \begin{bmatrix} \eta_0(\mathcal{L}_{lk})_{tan} & -(\mathcal{K}_{lk})_{tan} \\ (\mathcal{K}_{lk})_{tan} & 1/\eta_0(\mathcal{L}_{lk})_{tan} \end{bmatrix}. \qquad (2.55)$$

Note that, instead of Gram matrices, we use the left-hand side of (2.51). EPA versions using (2.29) and (2.51) are called normal EPA (N-EPA) and tangential (T-EPA), respectively, in the literature.

2.8 Numerical Results

As numerical examples, we first consider scattering from a PEC sphere of radius 1 m enclosed by an ES in the shape of a sphere of radius 1.5 m. The sphere is excited via a 1 V/m plane wave propagating along z direction with x polarized electric field at 100 MHz. The object is discretized by using the RWG functions as $\lambda/10$ triangles, where λ is the wavelength. The ES mesh is changed from $\lambda/5$ to $\lambda/30$ in order to observe the effect of the ES discretization. Far-zone electric field intensity is calculated with respect to bistatic angle on the xz plane. EFIE is used as the current solver in EPA and the relative error is calculated with respect to MoM-EFIE solutions. The relative error is defined as $|s_i - s_i^{\text{ref}}|/|s_i^{\text{ref}}|$, where s represents vector of sampled fields. Figure 2.4 presents the electric field intensity, while Figure 2.5 depicts the corresponding relative errors in EPA solutions. As it can be seen, the relative error decreases as the discretization of the ES becomes finer. This is important as it demonstrates the controllable accuracy of EPA.

Next, we consider a dielectric sphere with a relative permittivity $\epsilon_r = 4$ and λ diameter enclosed by a spherical ES with 1.5λ diameter at 1 GHz. The object is discretized with $\lambda/10$ triangles, while the ES is discretized with $\lambda/10$ and $\lambda/5$ triangles. The excitation is again a 1 V/m plane wave propagating in z direction with x polarized electric field. For the current solutions, (1.29) is used with different coefficients. Specially, by choosing proper coefficients, four different formulations, namely

combined tangential formulation (CTF), modified combined tangential formulation (MCTF), electric and magnetic current combined-field integral equation (JMCFIE), and Poggio–Miller–Chang–Harrington–Wu–Tsai (PMCHWT) formulations, are examined [23]. The bistatic far-zone electric field intensity is calculated and plotted in Figure 2.6. By comparing the results with those obtained via Mie-series solution, it can be seen that EPA solutions are consistent with MoM solutions, while they slightly deviate from Mie-series solutions depending on the inherent accuracy of the core formulation.
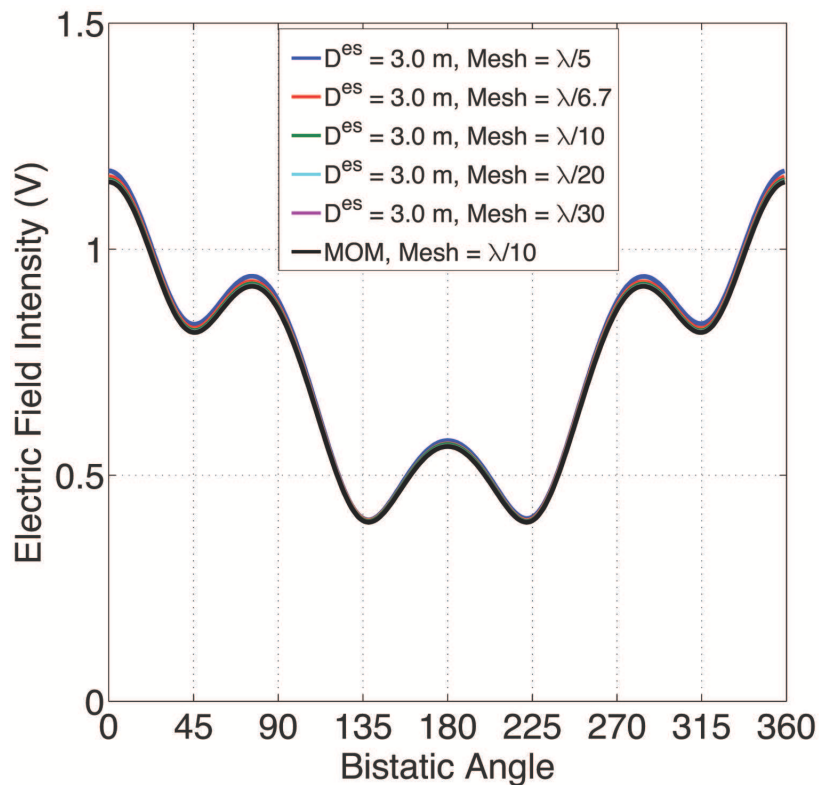

Figure 2.4: Scattering from a single PEC sphere of radius 1 m at 100 MHz. EPA is used with different discretizations for the ES surface of radius 1.5 m.
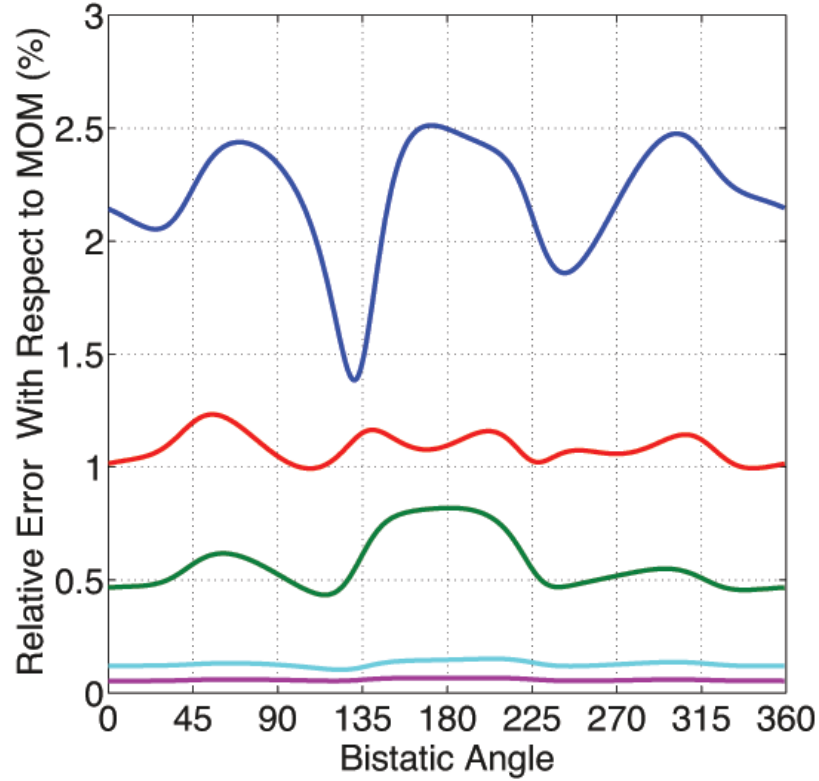
Figure 2.5: Relative error in the EPA solutions shown in Figure 2.4. The error is calculated with respect to MoM-EFIE. Here, the legends are same as the ones in Figure 2.4.

Finally, N-EPA and T-EPA solutions are compared. We consider scattering from a structure involving two PEC cubes with λ edge sizes and 2λ center-to-center distance at 300 MHz. ESs are also considered as cubes with 1.5λ edge sizes. The objects are discretized with 10 elements per edge (epe), while ESs are discretized with 3 to 10 elements per edge. The excitation is a y-polarized plane wave propagating along the negative z axis. The far-zone electric field intensities are calculated in xz plane with respect to bistatic angle. Figures 2.7 and 2.8 show that mesh convergence is observed for both cases (N-EPA and T-EPA). The forward-scattered radar cross section (RCS) is calculated with N-EPA, T-EPA, and MoM using the EFIE formulation. According to RCS results given in Figure 2.9, T-EPA has a better accuracy when the ESs are discretized with $\lambda/3$ or finer meshes.
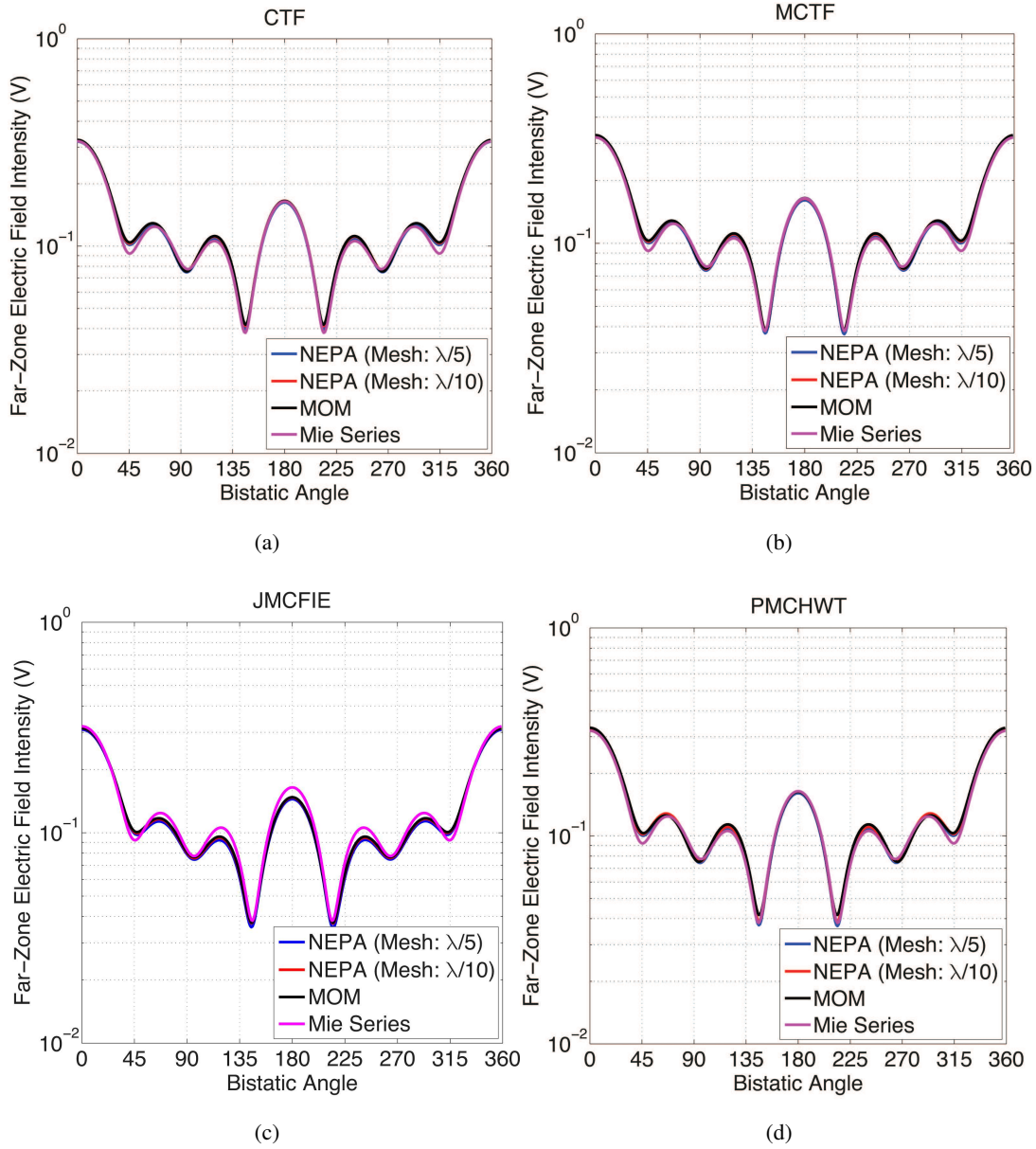
Figure 2.6: Solutions of scattering problems involving a dielectric sphere of diameter λ and relative permittivity $\epsilon_r = 4$. N-EPA and MoM are used for different formulations: (a) CTF, (b) MCTF, (c) JMCFIE, (d) PMCHWT.
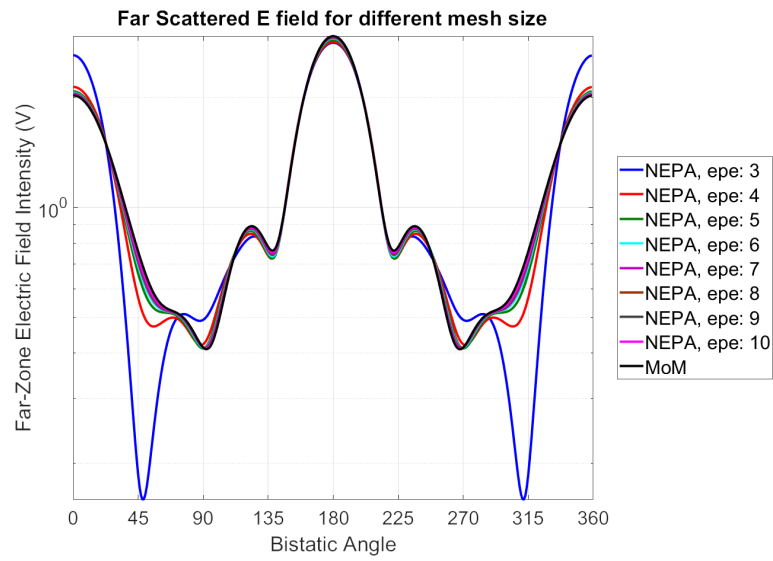
Figure 2.7: Far-zone electric field intensity of a structure involving two PEC cubes using N-EPA with different ES discretizations, in comparison to direct MoM.
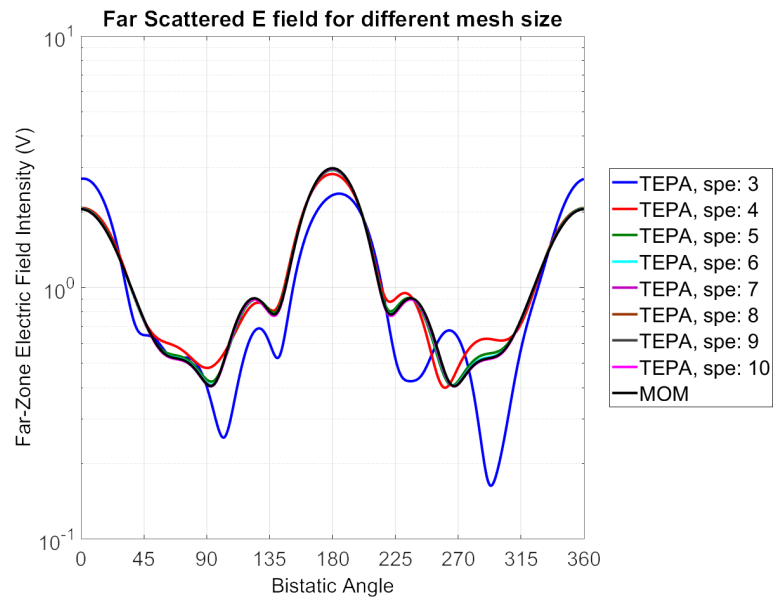
Figure 2.8: Far-zone electric field intensity of a structure involving two PEC cubes using T-EPA with different ES discretizations, in comparison to direct MoM.
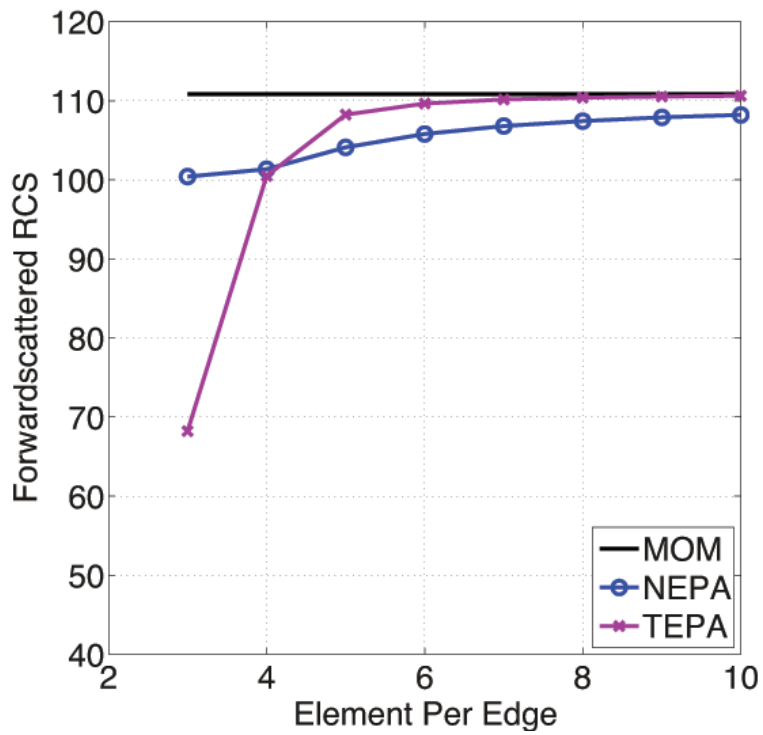
Figure 2.9: Forward-scattered RCS of a structure involving two PEC cubes using N-EPA, T-EPA, and MoM.

CHAPTER 3

ACCELERATION OF THE EQUIVALENCE PRINCIPLE ALGORITHM USING THE MULTILEVEL FAST MULTIPOLE ALGORITHM

3.1 Multilevel Fast Multipole Algorithm

As discussed in Chapter 1, using MoM for solving an electromagnetic problem leads to an $N \times N$ dense matrix equation with N unknowns. The complexity of solving such an equation using direct solvers, such as Gaussian elimination, is $\mathcal{O}(N^3)$. This makes the solution of large problems computationally expensive if not impossible. Faster solutions can be performed via iterative solvers, which require matrix-vector multiplications (MVMs) in order to generate subsequent guesses for the solution. A direct MVM in each iteration has $\mathcal{O}(N^2)$ complexity for both time and memory, which is still expensive for large problems. FMM and its multilevel version (MLFMA) can reduce time and memory complexity required for an MVM to $\mathcal{O}(N^{1.5})$ and $\mathcal{O}(N \log N)$, respectively, using the addition theorem. In MLFMA, the object is placed inside a cubic box and the box is recursively divided into smaller boxes for a total of $L = \mathcal{O}(\log N)$ levels. Then using a one-box-buffer scheme, all pairs of boxes at the same level are categorized as near-zone or far-zone. The interactions between basis and testing functions in nearby boxes are calculated directly, while the interactions of functions in far-zone are calculated in a group-by-group manner, based on the factorization of the Green's function using Gegenbauer's addition theorem.

3.1.1 Factorization of Green's Function

Using the Gegenbauer's addition theorem, the Green's function can be written as [1]

$$\frac{\exp(ik|\boldsymbol{w} + \boldsymbol{v}|)}{4\pi|\boldsymbol{w} + \boldsymbol{v}|} = \frac{ik}{4\pi}\sum_{t=0}^{\infty}(-1)^t(2t+1)j_t(kv)h_t^{(1)}(kw)P_t(\hat{\boldsymbol{w}} \cdot \hat{\boldsymbol{v}}), \tag{3.1}$$

where $\boldsymbol{w} + \boldsymbol{v} = \boldsymbol{r} - \boldsymbol{r}'$ and $|\boldsymbol{w}| = w > v = |\boldsymbol{v}|$, $j_t(kv)$ is the spherical Bessel function, $h_t^{(1)}(kv)$ is the first-kind spherical Hankel function, and P_t represents the Legendre polynomials. Spherical waves can be converted into plane waves as

$$j_t(kv)P_t(\hat{\boldsymbol{w}} \cdot \hat{\boldsymbol{v}}) = \frac{1}{4\pi(i)^t}\int d^2\hat{\boldsymbol{k}}\exp(ik\hat{\boldsymbol{k}} \cdot \boldsymbol{v})P_t(\hat{\boldsymbol{k}} \cdot \boldsymbol{w}), \tag{3.2}$$

where the integration is over the surface of unit sphere. Inserting (3.2) in (3.1), the diagonalized form of the Green's function can be derived as

$$\frac{\exp(ik|\boldsymbol{w} + \boldsymbol{v}|)}{4\pi|\boldsymbol{w} + \boldsymbol{v}|} = \frac{ik}{(4\pi)^2}\int d^2\hat{\boldsymbol{k}}\exp(ik\hat{\boldsymbol{k}} \cdot \boldsymbol{v})\sum_{t=0}^{\infty}(i)^t(2t+1)h_t^{(1)}(kw)P_t(\hat{\boldsymbol{k}} \cdot \hat{\boldsymbol{w}}).$$
$$\tag{3.3}$$

By defining shift and translation functions

$$\beta(\boldsymbol{k}, \boldsymbol{v}) = \exp(ik\hat{\boldsymbol{k}} \cdot \boldsymbol{v}) \tag{3.4}$$

$$\alpha(\boldsymbol{k}, \boldsymbol{w}) = \sum_{t=0}^{\infty}(i)^t(2t+1)h_t^{(1)}(kw)P_t(\hat{\boldsymbol{k}} \cdot \hat{\boldsymbol{w}}), \tag{3.5}$$

and truncating the summation in the translation function using a truncation number τ, (3.3) becomes

$$\frac{\exp(ik|\boldsymbol{w} + \boldsymbol{v}|)}{4\pi|\boldsymbol{w} + \boldsymbol{v}|} = \frac{ik}{(4\pi)^2}\int d^2\hat{\boldsymbol{k}}\beta(\boldsymbol{k}, \boldsymbol{v})\alpha_\tau(\boldsymbol{k}, \boldsymbol{w}). \tag{3.6}$$

In the implementation of MLFMA, the shift function is decomposed into multiple parts such as

$$\frac{\exp(ik|\boldsymbol{w} + \boldsymbol{v}|)}{4\pi|\boldsymbol{w} + \boldsymbol{v}|} = \frac{ik}{(4\pi)^2}\int d^2\hat{\boldsymbol{k}}\beta(\boldsymbol{k}, \boldsymbol{v}_1)\alpha_\tau(\boldsymbol{k}, \boldsymbol{w})\beta(\boldsymbol{k}, \boldsymbol{v}_2). \tag{3.7}$$

This way, an MVM involves three steps, known as aggregation, translation, and disaggregation.

As shown in Figure 3.1, in order to calculate the interactions between the elements of two far-zone boxes, the fields created by basis functions in the basis box are aggregated at its center using $\beta(\boldsymbol{k}, \boldsymbol{v}_1)$, then translated to the center of the testing box using $\alpha_\tau(\boldsymbol{k}, \boldsymbol{w})$, and finally, disaggregated onto testing functions using $\beta(\boldsymbol{k}, \boldsymbol{v}_2)$.
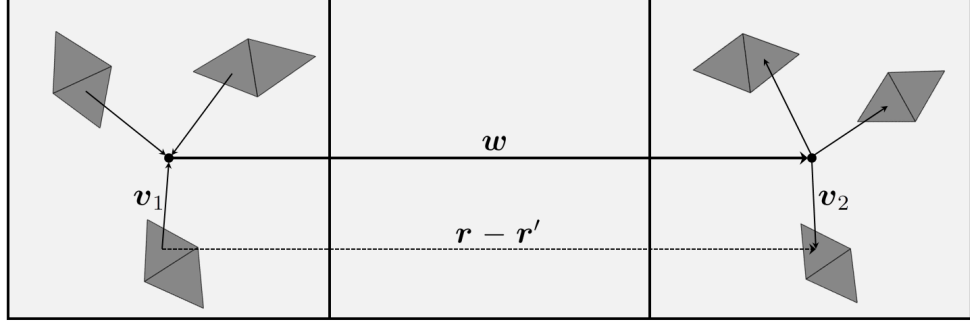
Figure 3.1: An illustration of group-by-group computations of interactions.

3.2 Applying MLFMA for MVMs in EPA

By considering (2.49), there are three operators involved in MVM using EPA. Both $\bar{U}_{ll}^{-1}$ and $\bar{S}_{ll}$ consist of direct inverses of matrices. Therefore only the translation operator $\mathcal{T}_{lk}$ can be calculated via MLFMA. In order to do this, the left-hand side of (2.46) is modified as

$$\left(\tilde{\bar{S}} \cdot \left(\bar{T} \cdot a^s \right)^\mathsf{T} \right)^\mathsf{T} + a^s, \tag{3.8}$$

where

$$\tilde{\bar{S}}_{lk} = \begin{cases} -\bar{U}_{ll}^{-1} \cdot \bar{S}_{ll} \cdot \bar{U}_{ll}^{-1} & , \quad l = k \\ 0 & , \quad l \neq k \end{cases} \tag{3.9}$$

$$\bar{T}_{lk} = \begin{cases} 0 & , \quad l = k \\ \bar{T}_{lk} & , \quad l \neq k \end{cases} \tag{3.10}$$

$$a^s = \begin{bmatrix} a_1^s \\ a_2^s \\ \vdots \\ a_L^s \end{bmatrix} . \tag{3.11}$$

In the above, $^\mathsf{T}$ represents the matrix transpose. Considering (2.45), the matrix of translation operators can be rewritten by rearranging its rows and columns as

$$
\begin{bmatrix}
0 & \bar{\boldsymbol{K}}_{12}^{N} & \cdots & \bar{\boldsymbol{K}}_{1L}^{N} & 0 & 1/\eta_0\bar{\boldsymbol{L}}_{12}^{N} & \cdots & 1/\eta_0\bar{\boldsymbol{L}}_{1L}^{N} \\
\bar{\boldsymbol{K}}_{21}^{N} & 0 & \cdots & \bar{\boldsymbol{K}}_{2L}^{N} & 1/\eta_0\bar{\boldsymbol{L}}_{21}^{N} & 0 & \cdots & 1/\eta_0\bar{\boldsymbol{L}}_{2L}^{N} \\
\vdots & \vdots & \ddots & \vdots & \vdots & \vdots & \ddots & \vdots \\
\bar{\boldsymbol{K}}_{L1}^{N} & \bar{\boldsymbol{K}}_{L2}^{N} & \cdots & 0 & 1/\eta_0\bar{\boldsymbol{L}}_{L1}^{N} & 1/\eta_0\bar{\boldsymbol{L}}_{L2}^{N} & \cdots & 0 \\
0 & -\eta_0\bar{\boldsymbol{L}}_{12}^{N} & \cdots & -\eta_0\bar{\boldsymbol{L}}_{1L}^{N} & 0 & \bar{\boldsymbol{K}}_{12}^{N} & \cdots & \bar{\boldsymbol{K}}_{1L}^{N} \\
-\eta_0\bar{\boldsymbol{L}}_{21}^{N} & 0 & \cdots & -\eta_0\bar{\boldsymbol{L}}_{2L}^{N} & \bar{\boldsymbol{K}}_{21}^{N} & 0 & \cdots & \bar{\boldsymbol{K}}_{2L}^{N} \\
\vdots & \vdots & \ddots & \vdots & \vdots & \vdots & \ddots & \vdots \\
-\eta_0\bar{\boldsymbol{L}}_{L1}^{N} & -\eta_0\bar{\boldsymbol{L}}_{L2}^{N} & \cdots & 0 & \bar{\boldsymbol{K}}_{L1}^{N} & \bar{\boldsymbol{K}}_{L2}^{N} & \cdots & 0
\end{bmatrix}
\cdot
\begin{bmatrix}
\boldsymbol{a}_{J_1}^{s} \\
\boldsymbol{a}_{J_2}^{s} \\
\vdots \\
\boldsymbol{a}_{J_L}^{s} \\
\boldsymbol{a}_{M_1}^{s} \\
\boldsymbol{a}_{M_2}^{s} \\
\vdots \\
\boldsymbol{a}_{M_L}^{s}
\end{bmatrix} . \quad (3.12)
$$

The MVM shown in (3.12) can be expressed in a simpler form as

$$
\begin{bmatrix}
\bar{\boldsymbol{K}}_{lk}^{N} & 1/\eta_0\bar{\boldsymbol{L}}_{lk}^{N} \\
-\eta_0\bar{\boldsymbol{L}}_{lk}^{N} & \bar{\boldsymbol{K}}_{lk}^{N}
\end{bmatrix}
\cdot
\begin{bmatrix}
\boldsymbol{a}_{J}^{s} \\
\boldsymbol{a}_{M}^{s}
\end{bmatrix} , \quad (3.13)
$$

where the self interaction of each ES has to be set to zero. After calculating (3.13) using MLFMA, by reordering the rows to the previous form, multiplying $\bar{\tilde{\boldsymbol{S}}}_{ll}$ with the corresponding rows, and finally adding to the coefficient vector, the left-hand side of (2.46) can be obtained. The procedure for TEPA is the same, and instead of (3.13) one needs to calculate

$$
\begin{bmatrix}
\eta_0\bar{\boldsymbol{L}}_{lk}^{T} & -\bar{\boldsymbol{K}}_{lk}^{T} \\
\bar{\boldsymbol{K}}_{lk}^{T} & 1/\eta_0\bar{\boldsymbol{L}}_{lk}^{T}
\end{bmatrix}
\cdot
\begin{bmatrix}
\boldsymbol{a}_{J}^{s} \\
\boldsymbol{a}_{M}^{s}
\end{bmatrix} . \quad (3.14)
$$

Inserting (3.7) in (1.39) to (1.42), the discretized $\mathcal{L}$ and $\mathcal{K}$ operators used in (3.13) and (3.14) can be written as

$$
\bar{\boldsymbol{L}}^{T}[m,n] = \left(\frac{ik}{4\pi}\right)^{2} \int d^2\hat{\boldsymbol{k}} \, \bar{\boldsymbol{F}}_m^{\mathcal{L},T}(\boldsymbol{k},\boldsymbol{r}_m) \cdot \alpha_\tau(\boldsymbol{k},\boldsymbol{r}_m - \boldsymbol{r}_n) \bar{\boldsymbol{S}}_n(\boldsymbol{k},\boldsymbol{r}_n) \quad (3.15)
$$

$$
\bar{\boldsymbol{L}}^{N}[m,n] = \left(\frac{ik}{4\pi}\right)^{2} \int d^2\hat{\boldsymbol{k}} \, \bar{\boldsymbol{F}}_m^{\mathcal{L},N}(\boldsymbol{k},\boldsymbol{r}_m) \cdot \alpha_\tau(\boldsymbol{k},\boldsymbol{r}_m - \boldsymbol{r}_n) \bar{\boldsymbol{S}}_n(\boldsymbol{k},\boldsymbol{r}_n) \quad (3.16)
$$

$$
\bar{\boldsymbol{K}}^{T}[m,n] = \left(\frac{ik}{4\pi}\right)^{2} \int d^2\hat{\boldsymbol{k}} \, \bar{\boldsymbol{F}}_m^{\mathcal{K},T}(\boldsymbol{k},\boldsymbol{r}_m) \cdot \alpha_\tau(\boldsymbol{k},\boldsymbol{r}_m - \boldsymbol{r}_n) \bar{\boldsymbol{S}}_n(\boldsymbol{k},\boldsymbol{r}_n) \quad (3.17)
$$

$$
\bar{\boldsymbol{K}}^{N}[m,n] = \left(\frac{ik}{4\pi}\right)^{2} \int d^2\hat{\boldsymbol{k}} \, \bar{\boldsymbol{F}}_m^{\mathcal{K},N}(\boldsymbol{k},\boldsymbol{r}_m) \cdot \alpha_\tau(\boldsymbol{k},\boldsymbol{r}_m - \boldsymbol{r}_n) \bar{\boldsymbol{S}}_n(\boldsymbol{k},\boldsymbol{r}_n), \quad (3.18)
$$

where $\boldsymbol{r}_m$ and $\boldsymbol{r}_n$ are position vectors representing the centers of testing and basis boxes. In the above, $\bar{\boldsymbol{F}}_m$ and $\bar{\boldsymbol{S}}_n$ are receiving and radiation patterns expressed in terms of the testing and basis functions, respectively, and they can be derived as

$$\bar{\boldsymbol{F}}_m^{\mathcal{L},T}(\boldsymbol{k},\boldsymbol{r}_m) = \int d\boldsymbol{r}\,\beta(\boldsymbol{k},\boldsymbol{r}-\boldsymbol{r}_m)(\bar{\boldsymbol{I}}_{3\times3} - \hat{\boldsymbol{k}}\hat{\boldsymbol{k}}) \cdot \boldsymbol{t}_m(\boldsymbol{r}) \tag{3.19}$$

$$\bar{\boldsymbol{F}}_m^{\mathcal{L},N}(\boldsymbol{k},\boldsymbol{r}_m) = \int d\boldsymbol{r}\,\beta(\boldsymbol{k},\boldsymbol{r}-\boldsymbol{r}_m)(\bar{\boldsymbol{I}}_{3\times3} - \hat{\boldsymbol{k}}\hat{\boldsymbol{k}}) \cdot \boldsymbol{t}_m(\boldsymbol{r}) \times \hat{\boldsymbol{n}} \tag{3.20}$$

$$\bar{\boldsymbol{F}}_m^{\mathcal{K},T}(\boldsymbol{k},\boldsymbol{r}_m) = -\hat{\boldsymbol{k}} \times \int d\boldsymbol{r}\,\beta(\boldsymbol{k},\boldsymbol{r}-\boldsymbol{r}_m)(\bar{\boldsymbol{I}}_{3\times3} - \hat{\boldsymbol{k}}\hat{\boldsymbol{k}}) \cdot \boldsymbol{t}_m(\boldsymbol{r}) \tag{3.21}$$

$$\bar{\boldsymbol{F}}_m^{\mathcal{K},N}(\boldsymbol{k},\boldsymbol{r}_m) = -\hat{\boldsymbol{k}} \times \int d\boldsymbol{r}\,\beta(\boldsymbol{k},\boldsymbol{r}-\boldsymbol{r}_m)(\bar{\boldsymbol{I}}_{3\times3} - \hat{\boldsymbol{k}}\hat{\boldsymbol{k}}) \cdot \boldsymbol{t}_m(\boldsymbol{r}) \times \hat{\boldsymbol{n}} \tag{3.22}$$

$$\bar{\boldsymbol{S}}_n(\boldsymbol{k},\boldsymbol{r}_n) = \int d\boldsymbol{r}\,\beta(\boldsymbol{k},\boldsymbol{r}_n-\boldsymbol{r})(\bar{\boldsymbol{I}}_{3\times3} - \hat{\boldsymbol{k}}\hat{\boldsymbol{k}}) \cdot \boldsymbol{b}_n(\boldsymbol{r}). \tag{3.23}$$

In equations (3.17) and (3.18), $\mathcal{K}$ operator does not include identity operator as the operators are defined for the calculation of far-zone interactions.

3.3 Numerical Results

In this section, two different electromagnetic problems involving periodic structures are presented. For both problems, solutions using N-EPA implementation accelerated by MLFMA are presented and compared with brute-force solutions via MoM and/or MLFMA.

First problem involves a microwave metamaterial array consisting of $3 \times 9 \times 9$ split-ring-resonator (SRR) elements. As it is depicted in Figure 3.2, a $3 \times 9 \times 9$ array of SRRs are arranged periodically in free space and centered at the origin. The periodicity of the array in x and y directions is 10.508 mm, while it is 18 mm in the z direction. The dimensions of a single element are shown in Figure 3.2 in detail. The SRRs are modeled as PEC elements with zero thickness. This geometry is used in [24] as part of a composite metamaterial and expected to resonate at frequencies between 5.25 GHz and 5.5 GHz. The array is excited via a Hertzian dipole. The dipole is y-directed and located at $x = 48$ mm.
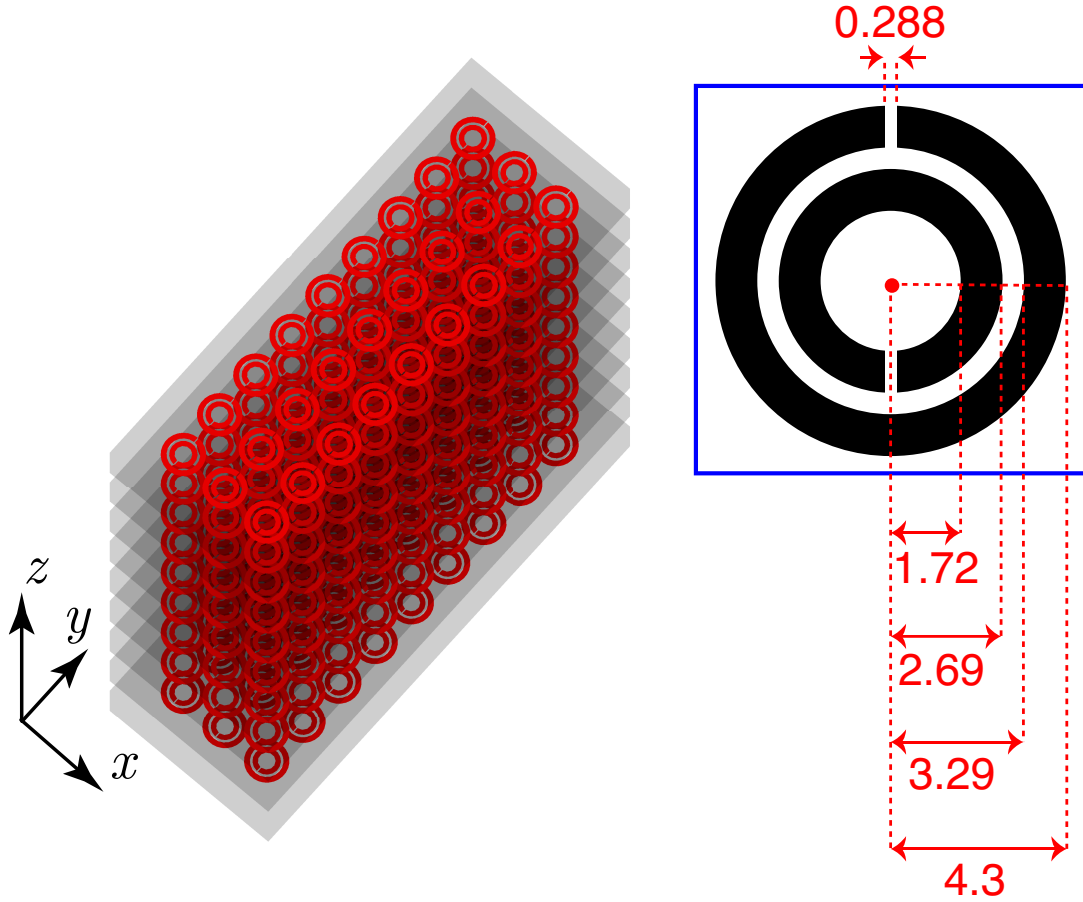
Figure 3.2: An array of $3 \times 9 \times 9$ SRRs that are arranged periodically. ESs that are used in EPA solutions are also shown. Dimensions are in millimeters.

For the problem described above, far-zone scattering is considered at nine discrete frequencies, i.e., between 4.5 GHz and 6.5 GHz with 250 MHz intervals. EFIE is used as the current solver and translations are calculated via MLFMA using 4 levels. SRRs are discretized by the RWG functions as 1 mm triangles, leading to 73 unknown functions per SRR. Therefore, the overall number of unknowns to discretize the array is 17739. For EPA solutions, each layer of SRRs are surrounded by a rectangular box, leading to a total of nine ESs. The dimensions of each box is 40 mm $\times 105$ mm $\times 12$ mm and the distance between them is 6 mm. ESs are also discretized by using the RWG functions as 5 mm triangles, leading to 1356 functions per ES and 12204 functions in total. Considering the fact that both electric and magnetic currents are defined as unknowns in EPA, the total number of unknowns is 24408. For comparisons, solutions are also performed by using a conventional MOM and a

standard MLFMA. All the iterative solutions are performed by using the generalized minimal residual method (GMRES) without restart or preconditioning. The error tolerance for GMRES is set to 10^{-4}. In Figure 3.3, far-zone scattered electric field is presented for frequencies 5.0 GHz and 5.5 GHz. The field amplitudes are plotted with respect to the bistatic angle on the x-z plane. It can be observed that, at these frequencies, MoM and EPA solutions are quite consistent with each other. However, it is clear that MLFMA results deviate from MoM and EPA results, particularly at 5.5 GHz. This error is caused by ill-conditioning of matrix equations at resonance frequencies. Figure 3.4 shows the number of GMRES iterations for different cases. It can be observed that iteration counts increase drastically at 5.25 GHz and 5.5 GHz due to the ill-conditioning of matrix equations at resonance frequencies, while it is under control when using EPA. As depicted in Figure 3.5, EPA reduces the solution time significantly, especially at 5.25 GHz and 5.5 GHz, in comparison to MoM and MLFMA. At 5.25 GHz, the speedup provided by EPA is 3.36 and 7.45 with respect to MoM and MLFMA. Finally, Figure 3.6 provides an overall plot for the relative errors in MLFMA and EPA solutions with respect to MoM. It can be observed that the error is mostly below 1 % for EPA, while it reaches almost 8 % for MLFMA.
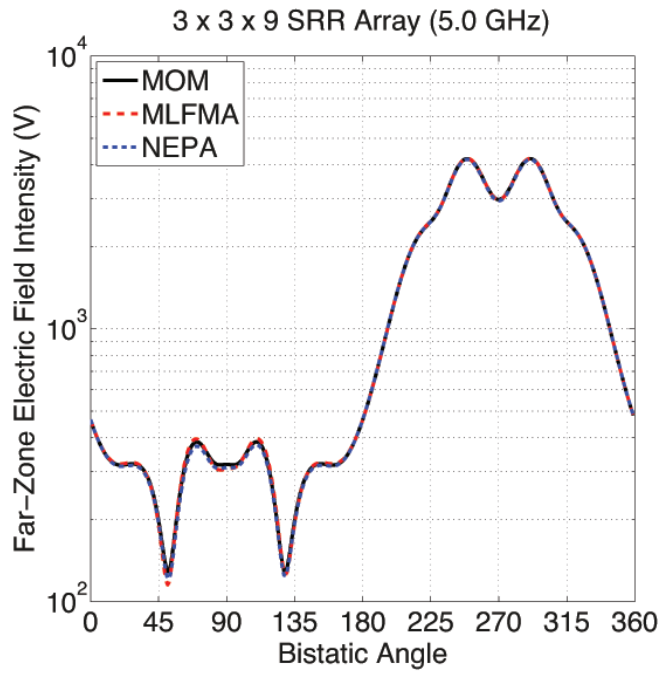
(a)
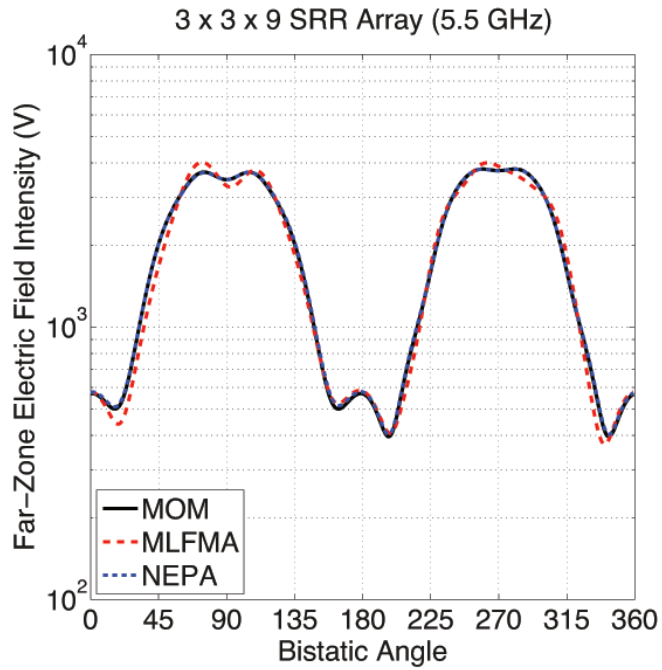
(b)

Figure 3.3: The far-zone electric field intensity obtained with three different solutions using MoM, MLFMA, and EPA at (a) 5.0 GHz and (b) 5.5 GHz.
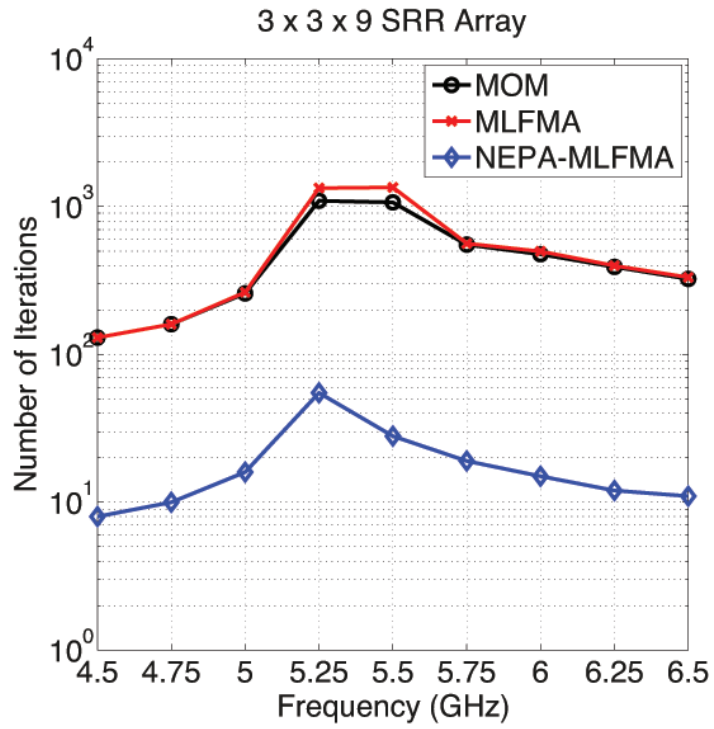
Figure 3.4: Number of GMRES iterations for three different solutions using MoM, MLFMA, and EPA at different frequency.
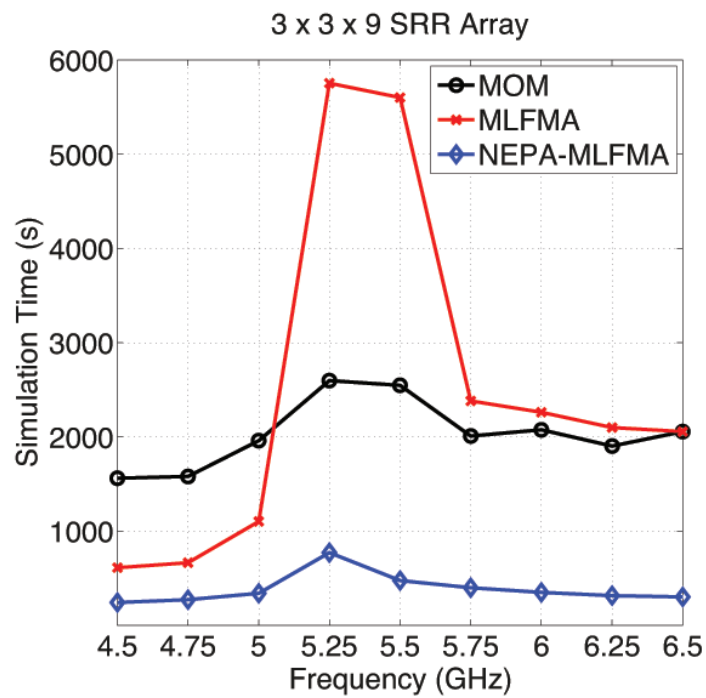

Figure 3.5: Total solution time for three different solutions using MoM, MLFMA, and EPA at different frequency.
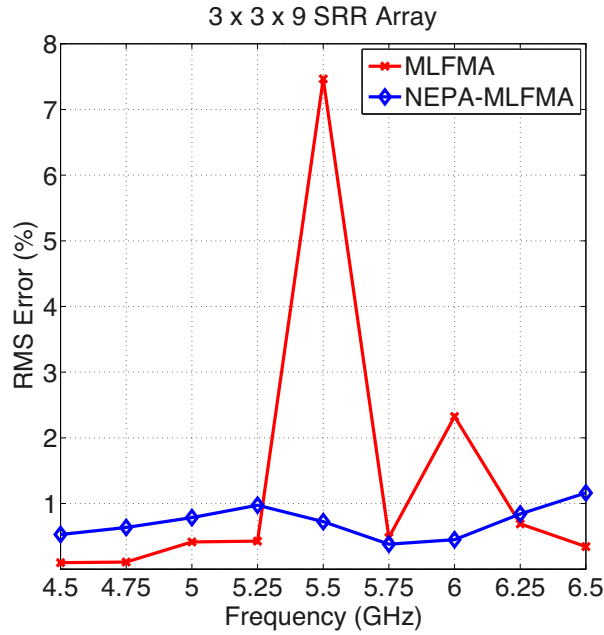
Figure 3.6: Relative errors in MLFMA and EPA solutions with respect to MoM.

The second problem we consider in this chapter is an array of 20×20 cage-dipole antennas located in free space. The antenna geometry used here is presented in [25] as an optimized antenna designed for radio-frequency-identification (RFID) application. The antennas are considered as PEC with the dimensions of 3.2 cm $\times$ 6.8 cm in x and y directions, respectively, and zero thickness. The periodicity of the array in x and y directions are 8 cm and 13 cm, respectively. The solution frequency is set to 2 GHz. Overall size of the structure is 1.57 m $\times$ 2.57 m which is larger than $10\lambda \times 17\lambda$, where λ is the operating wavelength. Problem setup is depicted in Figure 3.7. The array is excited by a plane wave propagating in the z direction with the electric field polarized in the x direction. Each array element is discretized with 521 RWG functions, which makes a total of 208400 unknowns to model the overall array. ESs are defined as rectangular boxes, each enclosing a single element. The ES dimensions are 5 cm $\times$ 10 cm $\times$ 2 cm and they are located symmetrically with respect to corresponding array elements. Each ES is discretized with 186 RWG functions, making a total of 148800 unknowns for the EPA solution. In Figure 3.8, far-zone electric field intensity in xz plane is depicted for EPA and MLFMA solutions, which are consistent with each other. Finally, in Figure 3.9, the residual error is plotted with respect to GMRES iterations for both EPA and MLFMA.
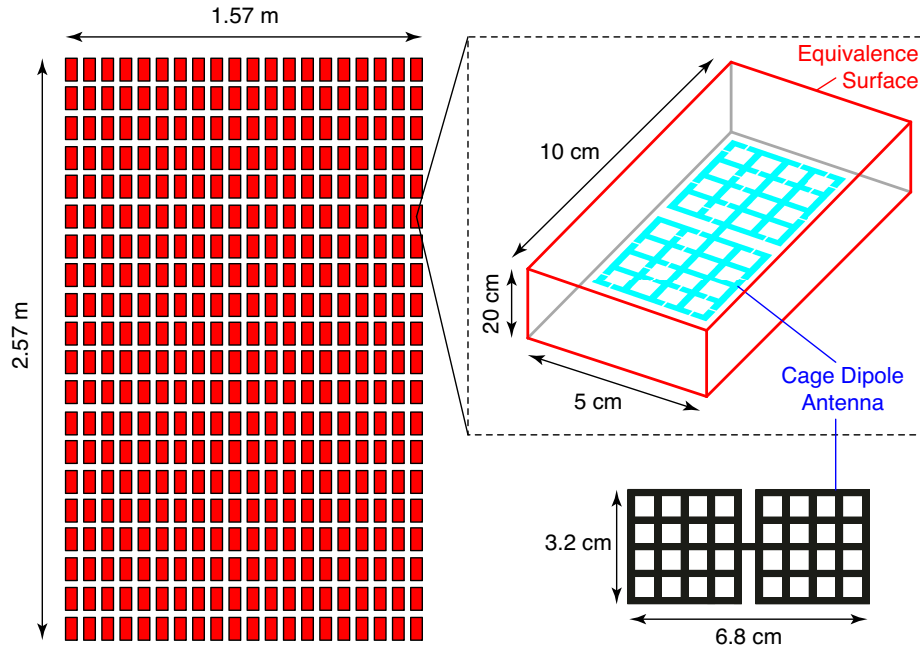
Figure 3.7: An array of 20 × 20 cage-dipole antennas. A representation of equivalence box used in the EPA solution is also depicted.
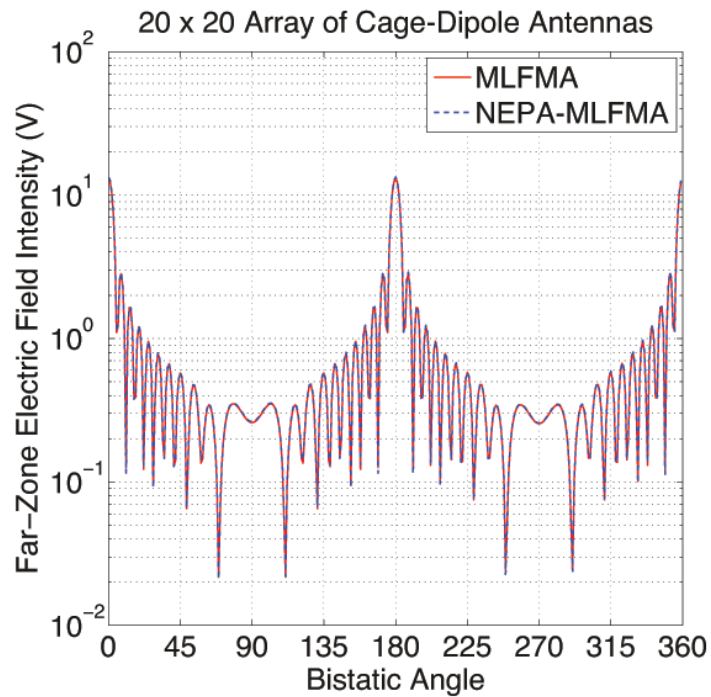
Figure 3.8: Electric field intensity in the far-zone scattered from antenna array in Figure 3.7
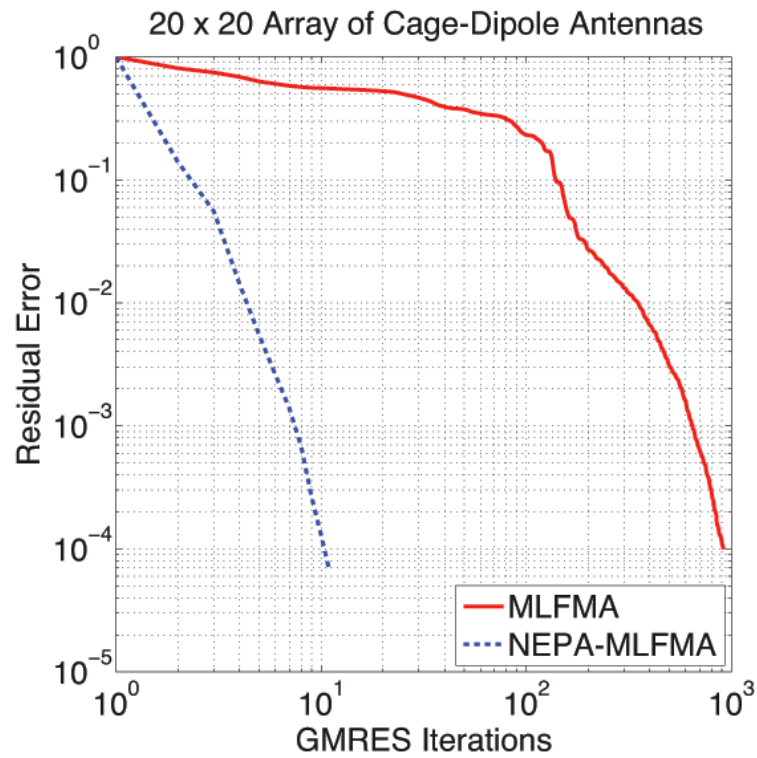
Figure 3.9: Convergence histories of iterative solutions.

The advantage of EPA is visible as improved convergence rate and reduced number of iterations. The total simulation time for MLFMA is 36726 seconds while it took only 1190 seconds for EPA to solve the same problem.

CHAPTER 4

EPA FOR POTENTIAL INTEGRAL EQUATIONS

Considering the results in the previous chapters, EPA has a noticeable efficiency when solving array structures. However, for multiscale problems, EPA suffers from low-frequency breakdowns due to fine discretizations of objects. These breakdowns are related to both applied formulations in subdomains and the operators used to project fields [26–28]. The main component causing a low-frequency breakdown is $\mathcal{L}$ defined in (1.16). To understand this in the context of PEC objects, the electric current $\boldsymbol{J}$ can be divided as solenoidal and irrotational parts. The solenoidal part is divergence-free and the irrotational part is curl-free; therefore, we have

$$\nabla \cdot \boldsymbol{J} = \nabla \cdot \boldsymbol{J}_{irr} \tag{4.1}$$

$$\nabla \times \boldsymbol{J} = \nabla \times \boldsymbol{J}_{sol}. \tag{4.2}$$

In the $\mathcal{L}$ operator, the first integral is due to the magnetic vector potential and it is a smooth operator that scales with frequency as $\mathcal{O}(\omega)$. The second one is due to the electric scalar potential and it contains a hyper-singular kernel, while depends on frequency as $\mathcal{O}(\omega^{-1})$. When the frequency approaches zero, the second term becomes dominant, and at one point, using finite precision, the solenoidal current is completely lost [26]. A common remedy for this issue is to separate contributions from vector and scalar potentials. Among many alternative choices to solve low-frequency problems, PIEs are considered in this thesis. In PIEs, equations are derived by applying boundary conditions for vector and scalar potentials, rather than fields. They employ the electric current density and the normal component of vector potential as unknowns, and they have very stable performances at low frequencies. In order to use PIEs for current solutions in EPA, proper equivalence principle expressions have to be utilized for potentials, as shown in this thesis.
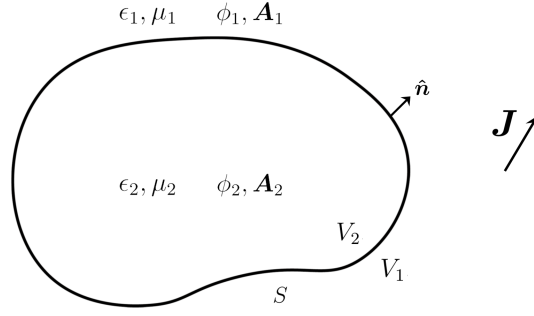
Figure 4.1: Problem setup used in the derivation of PIEs, where S defines the surface of the region 2.

4.1 Potential Integral Equations

PIEs are derived by using the Green's theorem starting with equations [13]

$$\nabla \times \nabla \times \boldsymbol{A}(\boldsymbol{r}) - \nabla \nabla \cdot \boldsymbol{A}(\boldsymbol{r}) - k^2 \boldsymbol{A}(\boldsymbol{r}) = \mu \boldsymbol{J}(\boldsymbol{r}) \tag{4.3}$$

$$\nabla \times \nabla \times \bar{\boldsymbol{G}}(\boldsymbol{r}, \boldsymbol{r}') - \nabla \nabla \cdot \bar{\boldsymbol{G}}(\boldsymbol{r}, \boldsymbol{r}') - k^2 \bar{\boldsymbol{G}}(\boldsymbol{r}, \boldsymbol{r}') = \bar{\boldsymbol{I}} \delta(\boldsymbol{r} - \boldsymbol{r}'). \tag{4.4}$$

Considering the problem setup illustrated in Figure 4.1, the magnetic vector potential in region 1 can be derived as

$$\left. \begin{array}{l} \boldsymbol{r} \in V_1, \ \boldsymbol{A}_1(\boldsymbol{r}) \\[2mm] \boldsymbol{r} \in V_2, \quad 0 \end{array} \right\} = \boldsymbol{A}^{\mathrm{i}}(\boldsymbol{r}) + \int_S d\boldsymbol{r}' \mu_1 g_1(\boldsymbol{r}, \boldsymbol{r}') \hat{\boldsymbol{n}}' \times \boldsymbol{H}_1(\boldsymbol{r}')$$

$$- \int_S d\boldsymbol{r}' \nabla' g_1(\boldsymbol{r}, \boldsymbol{r}') \times \hat{\boldsymbol{n}}' \times \boldsymbol{A}_1(\boldsymbol{r}')$$

$$- \int_S d\boldsymbol{r}' \hat{\boldsymbol{n}}' g_1(\boldsymbol{r}, \boldsymbol{r}') \nabla' \cdot \boldsymbol{A}_1(\boldsymbol{r}') \tag{4.5}$$

$$+ \int_S d\boldsymbol{r}' \hat{\boldsymbol{n}}' \cdot \boldsymbol{A}_1(\boldsymbol{r}') \nabla' g_1(\boldsymbol{r}, \boldsymbol{r}').$$

By taking divergence of both sides and using the Lorentz gauge ($\nabla \cdot \boldsymbol{A}(\boldsymbol{r}) = i\omega\epsilon\mu\phi(\boldsymbol{r})$) the electric scalar potential can be written as

$$\left. \begin{array}{l} \boldsymbol{r} \in V_1, \ \phi_1(\boldsymbol{r}) \\[2mm] \boldsymbol{r} \in V_2, \quad 0 \end{array} \right\} = \phi^{\mathrm{i}}(\boldsymbol{r}) + \int_S d\boldsymbol{r}' g_1(\boldsymbol{r}, \boldsymbol{r}') \hat{\boldsymbol{n}}' \cdot \boldsymbol{E}_1(\boldsymbol{r}')$$

$$- \nabla \cdot \int_S d\boldsymbol{r}' g_1(\boldsymbol{r}, \boldsymbol{r}') \hat{\boldsymbol{n}}' \phi_1(\boldsymbol{r}') \tag{4.6}$$

$$+ i\omega \int_S d\boldsymbol{r}' \hat{\boldsymbol{n}}' \cdot \boldsymbol{A}_1(\boldsymbol{r}') g_1(\boldsymbol{r}, \boldsymbol{r}').$$

42

Equations (4.5) and (4.6) can be considered as the equivalence principle for vector and scalar potentials. They state that, by knowing equivalent sources on the interface, potentials in the first region can be reproduced. For PEC scatterers, by applying boundary conditions and using the continuity equation, (4.5) and (4.6) are simplified to

$$-\hat{\boldsymbol{n}} \times \boldsymbol{A}^{\mathrm{i}}(\boldsymbol{r}) = \hat{\boldsymbol{n}} \times \int_S d\boldsymbol{r}' \mu \boldsymbol{J}(\boldsymbol{r}') g_1(\boldsymbol{r}, \boldsymbol{r}') + \hat{\boldsymbol{n}} \times \int_S d\boldsymbol{r}' \hat{\boldsymbol{n}}' \cdot \boldsymbol{A}(\boldsymbol{r}') \nabla' g_1(\boldsymbol{r}, \boldsymbol{r}') \quad (4.7)$$

$$-i\omega\epsilon\phi^{\mathrm{i}}(\boldsymbol{r}) = \int_S d\boldsymbol{r}' \nabla' \cdot \boldsymbol{J}(\boldsymbol{r}') g_1(\boldsymbol{r}, \boldsymbol{r}') + \omega^2 \epsilon \int_S d\boldsymbol{r}' \hat{\boldsymbol{n}}' \cdot \boldsymbol{A}(\boldsymbol{r}') g_1(\boldsymbol{r}, \boldsymbol{r}'). \quad (4.8)$$

In [16], a breakdown of PIEs for extremely low frequencies have been investigated and a remedy is introduced by calculating $\hat{\boldsymbol{n}} \cdot \nabla\phi$ on the surface. Then employing electric charge density, which can be derived by using $\hat{\boldsymbol{n}} \cdot \boldsymbol{A}$ and $\hat{\boldsymbol{n}} \cdot \nabla\phi$, fields can be calculated accurately at extremely low frequencies. In (4.6), by combining the first and the last integrals, while setting the second integral to zero due to the PEC boundary conditions, the required equation for $\hat{\boldsymbol{n}} \cdot \nabla\phi$ can be derived as

$$\phi^{\mathrm{i}}(\boldsymbol{r}) = \int d\boldsymbol{r}' \hat{\boldsymbol{n}}' \cdot \nabla'\phi(\boldsymbol{r}') g(\boldsymbol{r}, \boldsymbol{r}'). \quad (4.9)$$

This equations is also used in the context of EPA.

4.2 EPA operators for PIEs

Considering the equivalence principles for fields and potentials, electric and magnetic currents, electric and magnetic charges, normal and rotated tangential components of magnetic vector potential, and the electric scalar potential can be defined as equivalent sources. For simplicity, extra operators used when expressing the EPA operators are

43

defined as

$$\mathcal{V}\{\boldsymbol{X}\}(\boldsymbol{r}) = \int d\boldsymbol{r}' \boldsymbol{X}(\boldsymbol{r}') g(\boldsymbol{r}, \boldsymbol{r}') \qquad (4.10)$$

$$\mathcal{F}\{\boldsymbol{X}\}(\boldsymbol{r}) = \int d\boldsymbol{r}' \nabla' \cdot \boldsymbol{X}(\boldsymbol{r}') g(\boldsymbol{r}, \boldsymbol{r}') \qquad (4.11)$$

$$\mathcal{M}\{X\}(\boldsymbol{r}) = \int d\boldsymbol{r}' X(\boldsymbol{r}') \hat{\boldsymbol{n}}' \cdot \nabla' g(\boldsymbol{r}, \boldsymbol{r}') \qquad (4.12)$$

$$\mathcal{N}\{X\}(\boldsymbol{r}) = \int d\boldsymbol{r}' X(\boldsymbol{r}') g(\boldsymbol{r}, \boldsymbol{r}') \qquad (4.13)$$

$$\mathcal{C}\{X\}(\boldsymbol{r}) = \int d\boldsymbol{r}' \hat{\boldsymbol{n}}' X(\boldsymbol{r}') g(\boldsymbol{r}, \boldsymbol{r}') \qquad (4.14)$$

$$\mathcal{E}\{X\}(\boldsymbol{r}) = \int d\boldsymbol{r}' X(\boldsymbol{r}') \nabla g(\boldsymbol{r}, \boldsymbol{r}'). \qquad (4.15)$$

Employing these operators, in addition to those defined in Chapter 1, fields and potentials can be expressed in terms of equivalent sources on ESs. The equivalent sources are considered as

$$\boldsymbol{C}_l^{\text{s/i}} = \begin{bmatrix} \boldsymbol{J}_{H,l}^{\text{s/i}} \\ \boldsymbol{M}_l^{\text{s/i}} \\ \boldsymbol{J}_{A,l}^{\text{s/i}} \\ \rho_{e,l}^{\text{s/i}} \\ \rho_{m,l}^{\text{s/i}} \\ \Phi_l^{\text{s/i}} \\ \Sigma_l^{\text{s/i}} \end{bmatrix} = \begin{bmatrix} \hat{\boldsymbol{n}}_l \times \boldsymbol{H}^{\text{s/i}} \\ \hat{\boldsymbol{n}}_l \times \boldsymbol{E}^{\text{s/i}} \\ \hat{\boldsymbol{n}}_l \times \boldsymbol{A}^{\text{s/i}} \\ \hat{\boldsymbol{n}}_l \cdot \boldsymbol{E}^{\text{s/i}} \\ \hat{\boldsymbol{n}}_l \cdot \boldsymbol{H}^{\text{s/i}} \\ \nabla \cdot \boldsymbol{A}^{\text{s/i}} \\ \hat{\boldsymbol{n}}_l \cdot \boldsymbol{A}^{\text{s/i}} \end{bmatrix}. \qquad (4.16)$$

The scattering operator can be described as before by using product of three operators. Outside-in operator is defined to create incident potentials from equivalent sources using (4.5) and (4.6). Then PIEs are employed to solve the problem within each subdomain, and inside-out operator projects the electric current and the normal component of vector potential on ES to create secondary equivalent sources. Finally, the translation operator is defined to calculate the interactions between subdomains. The scattering operator can be written as

$$\boldsymbol{S}_{ll} = \boldsymbol{C}_{lp} \cdot \boldsymbol{R}_{pp} \cdot (\boldsymbol{B}_{pp})^{-1} \cdot \boldsymbol{A}_{pl}, \qquad (4.17)$$

44

where

$$
\mathcal{A}_{pl} = \begin{bmatrix} \mu\mathcal{V} & 0 & \mathcal{K} & 0 & 0 & -\mathcal{C} & \mathcal{E} \\ 0 & 0 & 0 & i\omega\epsilon\mathcal{N} & 0 & 1/\mu\mathcal{M} & \omega^2\epsilon\mathcal{N} \\ 0 & 0 & 0 & i\omega\epsilon\mathcal{N} & 0 & 1/\mu\mathcal{M} & \omega^2\epsilon\mathcal{N} \end{bmatrix} \tag{4.18}
$$

$$
\mathcal{B}_{pp} = \begin{bmatrix} \mu\mathcal{V} & \mathcal{E} & 0 \\ \mathcal{F} & \omega^2\epsilon\mathcal{N} & 0 \\ 0 & 0 & -i\omega\epsilon\mathcal{N} \end{bmatrix} \tag{4.19}
$$

$$
\mathcal{C}_{lp} = \begin{bmatrix} \hat{\boldsymbol{n}} \times \mathcal{K} & 0 & 0 \\ i\omega\mu\hat{\boldsymbol{n}} \times \mathcal{V} & 0 & 1/\epsilon\hat{\boldsymbol{n}} \times \mathcal{E} \\ \mu\hat{\boldsymbol{n}} \times \mathcal{V} & \hat{\boldsymbol{n}} \times \mathcal{E} & 0 \\ i\omega\mu\hat{\boldsymbol{n}} \cdot \mathcal{V} & 0 & 1/\epsilon\hat{\boldsymbol{n}} \cdot \mathcal{E} \\ \hat{\boldsymbol{n}} \cdot \mathcal{K} & 0 & 0 \\ 0 & \omega^2\mu\epsilon\mathcal{N} & i\omega\mu\mathcal{N} \\ \mu\hat{\boldsymbol{n}} \cdot \mathcal{V} & \hat{\boldsymbol{n}} \cdot \mathcal{E} & 0 \end{bmatrix} \tag{4.20}
$$

$$
\mathcal{R}_{pp} = \begin{bmatrix} \boldsymbol{I} & 0 & 0 \\ 0 & \boldsymbol{I} & 0 \\ 0 & i\omega\epsilon\boldsymbol{I} & -\epsilon\boldsymbol{I} \end{bmatrix}. \tag{4.21}
$$

Here (4.21) combines $\hat{\boldsymbol{n}} \cdot \boldsymbol{A}$ and $\hat{\boldsymbol{n}} \cdot \nabla\phi$ in order to create $\hat{\boldsymbol{n}} \cdot \boldsymbol{E}$. The translation operator can be defined as

$$
\mathcal{T}_{lk} = \begin{bmatrix} \hat{\boldsymbol{n}} \times \mathcal{K} & -i\omega\epsilon\hat{\boldsymbol{n}} \times \mathcal{V} & 0 & 0 & \hat{\boldsymbol{n}} \times \mathcal{E} & 0 & 0 \\ i\omega\mu\hat{\boldsymbol{n}} \times \mathcal{V} & \hat{\boldsymbol{n}} \times \mathcal{K} & 0 & \hat{\boldsymbol{n}} \times \mathcal{E} & 0 & 0 & 0 \\ \mu\hat{\boldsymbol{n}} \times \mathcal{V} & 0 & \hat{\boldsymbol{n}} \times \mathcal{K} & 0 & 0 & -\hat{\boldsymbol{n}} \times \mathcal{C} & \hat{\boldsymbol{n}} \times \mathcal{E} \\ i\omega\mu\hat{\boldsymbol{n}} \cdot \mathcal{V} & \hat{\boldsymbol{n}} \cdot \mathcal{K} & 0 & \hat{\boldsymbol{n}} \cdot \mathcal{E} & 0 & 0 & 0 \\ \hat{\boldsymbol{n}} \cdot \mathcal{K} & -i\omega\epsilon\hat{\boldsymbol{n}} \cdot \mathcal{V} & 0 & 0 & \hat{\boldsymbol{n}} \cdot \mathcal{E} & 0 & 0 \\ 0 & 0 & 0 & i\omega\mu\epsilon\mathcal{N} & 0 & \mathcal{M} & \omega^2\mu\epsilon\mathcal{N} \\ \mu\hat{\boldsymbol{n}} \cdot \mathcal{V} & 0 & \hat{\boldsymbol{n}} \cdot \mathcal{K} & 0 & 0 & -\hat{\boldsymbol{n}} \cdot \mathcal{C} & \hat{\boldsymbol{n}} \cdot \mathcal{E} \end{bmatrix}. \tag{4.22}
$$

Discretization of operators can be performed as described in Chapter 1. For this purpose, the RWG and pulse functions are used in order to expand vector and scalar functions. Operators used in scattering and translation operators can be discretized as

$$\bar{\boldsymbol{V}}^T[m,n] = \int_{S_m} d\boldsymbol{r} \boldsymbol{t}_m^{\text{RWG}}(\boldsymbol{r}) \cdot \int_{S_n} d\boldsymbol{r}' \boldsymbol{b}_n^{\text{RWG}}(\boldsymbol{r}') g(\boldsymbol{r},\boldsymbol{r}') \tag{4.23}$$

$$\bar{\boldsymbol{V}}^N[m,n] = \int_{S_m} d\boldsymbol{r} \boldsymbol{t}_m^{\text{RWG}}(\boldsymbol{r}) \cdot \hat{\boldsymbol{n}} \times \int_{S_n} d\boldsymbol{r}' \boldsymbol{b}_n^{\text{RWG}}(\boldsymbol{r}') g(\boldsymbol{r},\boldsymbol{r}') \tag{4.24}$$

$$\bar{\boldsymbol{V}}^n[p,n] = \int_{S_p} d\boldsymbol{r} t_p^{\text{PLS}}(\boldsymbol{r}) \hat{\boldsymbol{n}} \cdot \int_{S_n} d\boldsymbol{r}' \boldsymbol{b}_n^{\text{RWG}}(\boldsymbol{r}') g(\boldsymbol{r},\boldsymbol{r}') \tag{4.25}$$

$$\bar{\boldsymbol{F}}^T[p,n] = \int_{S_p} d\boldsymbol{r} t_p^{\text{PLS}}(\boldsymbol{r}) \int_{S_n} d\boldsymbol{r}' \nabla' \cdot \boldsymbol{b}_n^{\text{RWG}}(\boldsymbol{r}') g(\boldsymbol{r},\boldsymbol{r}') \tag{4.26}$$

$$\bar{\boldsymbol{M}}^T[m,q] = \int_{S_p} d\boldsymbol{r} t_p^{\text{PLS}}(\boldsymbol{r}) \int_{S_q} d\boldsymbol{r}' b_q^{\text{PLS}}(\boldsymbol{r}') \hat{\boldsymbol{n}}' \cdot \nabla' g(\boldsymbol{r},\boldsymbol{r}') \tag{4.27}$$

$$\bar{\boldsymbol{N}}^T[p,q] = \int_{S_p} d\boldsymbol{r} t_p^{\text{PLS}}(\boldsymbol{r}) \int_{S_q} d\boldsymbol{r}' b_q^{\text{PLS}}(\boldsymbol{r}') g(\boldsymbol{r},\boldsymbol{r}') \tag{4.28}$$

$$\bar{\boldsymbol{C}}^T[m,q] = \int_{S_m} d\boldsymbol{r} \boldsymbol{t}_m^{\text{RWG}}(\boldsymbol{r}) \cdot \int_{S_q} d\boldsymbol{r}' \hat{\boldsymbol{n}}' b_q^{\text{PLS}}(\boldsymbol{r}') g(\boldsymbol{r},\boldsymbol{r}') \tag{4.29}$$

$$\bar{\boldsymbol{E}}^T[m,q] = \int_{S_m} d\boldsymbol{r} \nabla \cdot \boldsymbol{t}_m^{\text{RWG}}(\boldsymbol{r}) \int_{S_q} d\boldsymbol{r}' b_q^{\text{PLS}}(\boldsymbol{r}') g(\boldsymbol{r},\boldsymbol{r}') \tag{4.30}$$

$$\bar{\boldsymbol{E}}^N[m,q] = \int_{S_m} d\boldsymbol{r} \boldsymbol{t}_m^{\text{RWG}}(\boldsymbol{r}) \cdot \hat{\boldsymbol{n}} \times \int_{S_q} d\boldsymbol{r}' b_q^{\text{PLS}}(\boldsymbol{r}') \nabla' g(\boldsymbol{r},\boldsymbol{r}') \tag{4.31}$$

$$\bar{\boldsymbol{E}}^n[p,q] = \int_{S_p} d\boldsymbol{r} t_p^{\text{PLS}}(\boldsymbol{r}) \hat{\boldsymbol{n}} \cdot \int_{S_q} d\boldsymbol{r}' b_q^{\text{PLS}}(\boldsymbol{r}') \nabla' g(\boldsymbol{r},\boldsymbol{r}') \tag{4.32}$$

$$\bar{\boldsymbol{K}}^T[m,n] = \int_{S_m} d\boldsymbol{r} \boldsymbol{t}_m^{\text{RWG}}(\boldsymbol{r}) \cdot \int_{S_n} d\boldsymbol{r}' \boldsymbol{b}_n^{\text{RWG}}(\boldsymbol{r}') \times \nabla' g(\boldsymbol{r},\boldsymbol{r}') \tag{4.33}$$

$$\bar{\boldsymbol{K}}^N[m,n] = \int_{S_m} d\boldsymbol{r} \boldsymbol{t}_m^{\text{RWG}}(\boldsymbol{r}) \cdot \hat{\boldsymbol{n}} \times \int_{S_n} d\boldsymbol{r}' \boldsymbol{b}_n^{\text{RWG}}(\boldsymbol{r}') \times \nabla' g(\boldsymbol{r},\boldsymbol{r}') \tag{4.34}$$

$$\bar{\boldsymbol{K}}^n[p,n] = \int_{S_p} d\boldsymbol{r} t_p^{\text{PLS}}(\boldsymbol{r}) \hat{\boldsymbol{n}} \cdot \int_{S_n} d\boldsymbol{r}' \boldsymbol{b}_n^{\text{RWG}}(\boldsymbol{r}') \times \nabla' g(\boldsymbol{r},\boldsymbol{r}'). \tag{4.35}$$

In these expressions, pulse functions are defined as

$$b_q^{\text{PLS}}(\boldsymbol{r}) = \begin{cases} 1, & \boldsymbol{r} \in S_q \\ 0, & \boldsymbol{r} \notin S_q \end{cases}. \tag{4.36}$$

4.3 Excitation

As (4.16) suggests, for solving problems with PIEs, incident potentials are also required in addition to incident fields. Equation (4.8) is derived by taking the divergence

of (4.7) and using the Lorentz gauge. This means that the incident fields should also satisfy the Lorentz gauge. In [14], it has been shown that enforcing Lorentz gauge does not impose uniqueness on the potentials. For plane waves, potentials can be defined as

$$
\begin{cases}
\boldsymbol{A}^{\mathrm{i}} = \dfrac{1}{i\omega}\boldsymbol{E}^{\mathrm{i}} \\
\phi^{\mathrm{i}} = 0,
\end{cases}
\tag{4.37}
$$

while this form is not stable at low frequencies since the vector potential becomes unbounded as $\omega \to 0$. Considering the electric field defined in (2.20), a stable form of potentials can be defined as

$$
\begin{cases}
\boldsymbol{A}^{\mathrm{i}} = -\hat{\boldsymbol{k}}(\boldsymbol{r} \cdot \hat{\boldsymbol{e}})E_a\sqrt{\mu\epsilon}\exp ik\hat{\boldsymbol{k}} \cdot \boldsymbol{r} \\
\phi^{\mathrm{i}} = -\boldsymbol{r} \cdot \hat{\boldsymbol{e}}E_a \exp ik\hat{\boldsymbol{k}} \cdot \boldsymbol{r}.
\end{cases}
\tag{4.38}
$$

It can be shown that these potential expressions satisfy the Lorentz gauge and they represents plane waves.

4.4 Numerical Results

In this section, we start with numerical results verifying the equivalence principle for vector and scalar potentials. Then, solutions of single-sphere problems using EPA-PIE are considered in comparison to analytical solutions (Mie-series solutions). Finally, an array of spheres is analyzed at different frequencies in order to demonstrate the stability of EPA-PIE at low frequencies.

In order to investigate the equivalence principle for vector and scalar potentials given in (4.5) and (4.6), we consider a plane wave in free space propagating in the z direction with x-polarized electric field. A hypothetical sphere of diameter λ discretized with $\lambda/10$ triangles is located at the origin. The purpose is to show that vector and scalar potentials associated with the plane wave can be recreated by using the equivalent sources given in (4.5) and (4.6). As mentioned in the previous section, two different pairs of potentials can be used for plane waves. Here we use the pair given in (4.38). After calculating the equivalent sources, we radiate them using (4.5) and (4.6). Figure 4.2 depicts the numerical potentials as well as the analytical ones, where good agreement is observed.
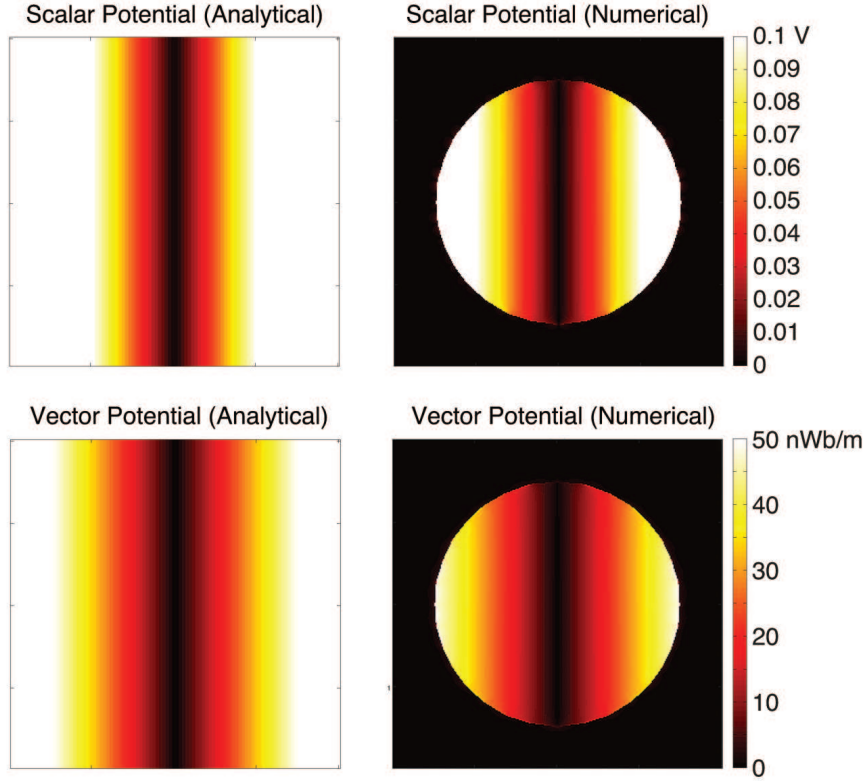
Figure 4.2: Potentials calculated via the equivalence principle in comparison to analytical plots.

Next, we consider a PEC sphere with of 0.15 m centered at the origin and enclosed by a spherical ES of radius 0.25 m. The object and ES are discretized with 2 cm and 3 cm triangles, respectively. The excitation is again a plane wave propagating in the z direction with x-polarized electric field. Iterative solutions are performed with 10^{-3} and 10^{-5} relative-error tolerances. Figures 4.3a and 4.3b show the far-zone electric field intensity at 1 MHz and 10 kHz. Beside EPA-PIE, PIE and EFIE are used for comparisons, while Mie-series solutions are used as reference. We observe that, at 1 MHz and for the 10^{-3} case, PIE and EPA-PIE provide accurate results that are consistent with Mie series, while relative errors (defined as $\|s - s^{\mathrm{ref}}\|_2/\|s^{\mathrm{ref}}\|$, where s is the field vectors) are less than 1%. However, EFIE gives inaccurate scattering values with its typically incorrect dip at a shifted angle. At this frequency, EFIE can be enforced to be accurate by reducing the GMRES tolerance to 10^{-5}. On the other hand, considering the same scenario for 10 kHz, EFIE becomes inaccurate in both cases, while PIE and EPA-PIE retain the accuracy and the target error level of 1%.
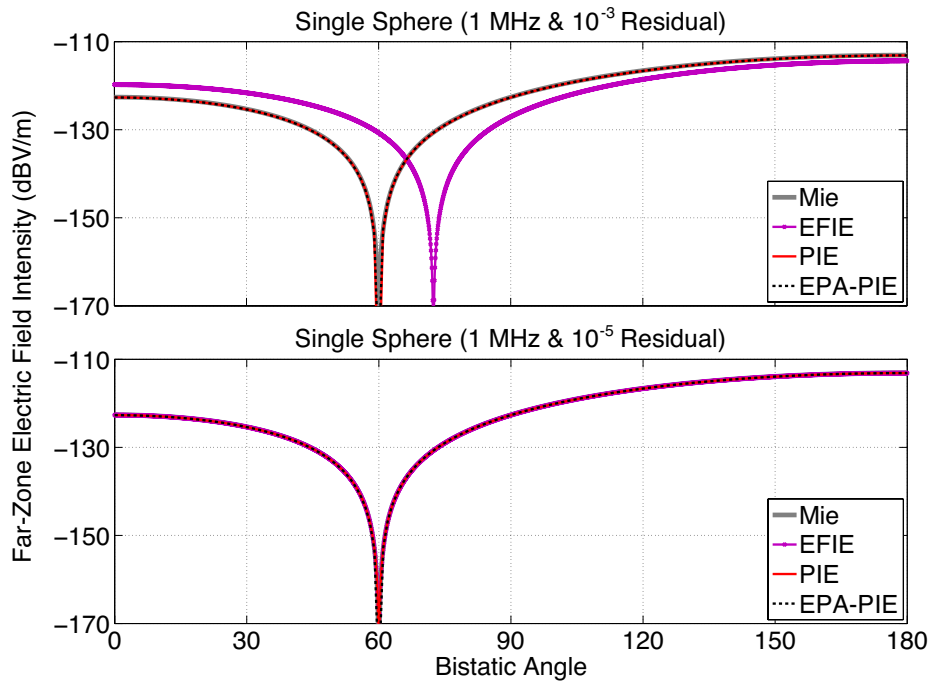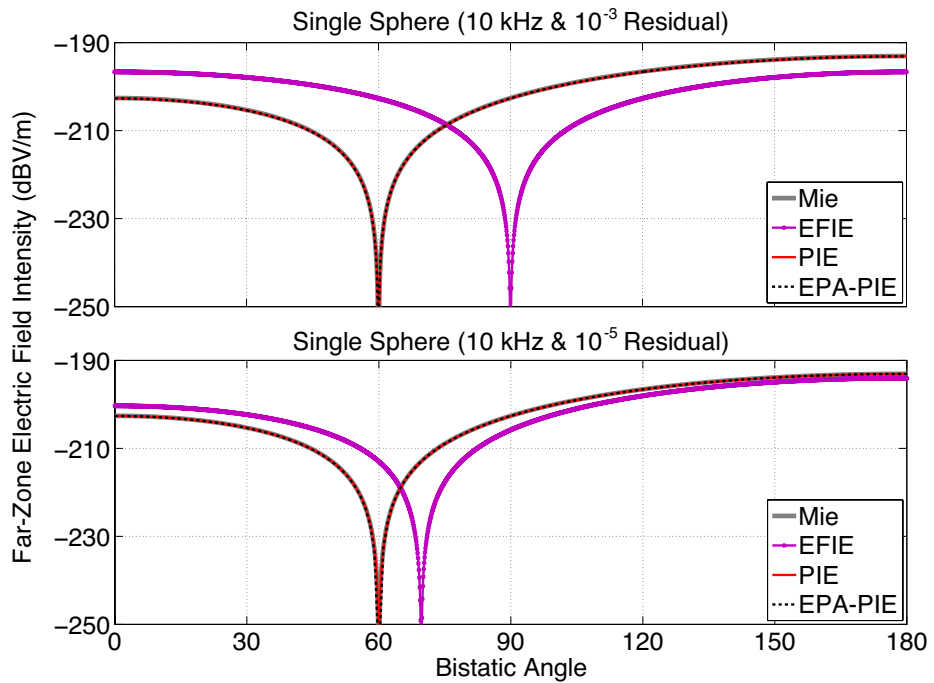
Figure 4.3: Solutions of scattering from single sphere of radius 0.15 m at (a) 1 MHz and (b) 10 kHz.

In order to visualize how EPA-PIE works, fields and potentials near the sphere are calculated at 1 MHz. Figures 4.4 and 4.5 depict near-zone fields and potentials created by equivalent sources on the object found by using PIEs. Figures 4.6 and 4.7 illustrate near-zone fields and potentials created by equivalent sources on the ES obtained with EPA-PIE. The followings can be observed:

- Outside the ES: The results of PIE and EPA-PIE are consistent with each other for both scattered and total fields, as well as potentials.

- Inside the ES: For EPA-PIE, the scattered fields and potentials created from equivalent sources on the ES are zero, as expected from Huygens' principle. Hence, the total fields and potentials created by the same sources are incident fields and potentials.

- Inside the Object: For PIEs, the scattered fields and potentials created from equivalent sources on the object are correctly negative of incident fields and potentials, since the total fields and potentials must be zero inside PEC objects.
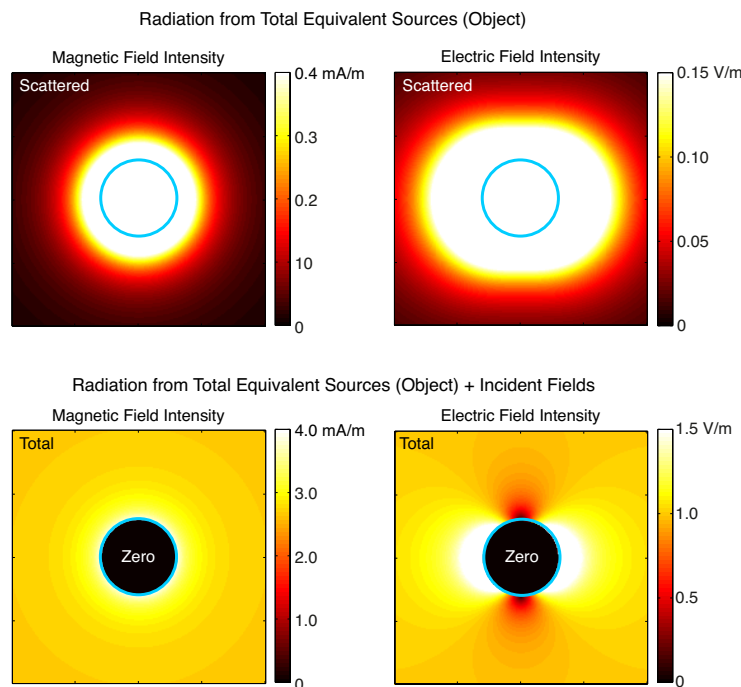

Figure 4.4: Fields created by equivalent sources on the object obtained by using PIEs for a single sphere.
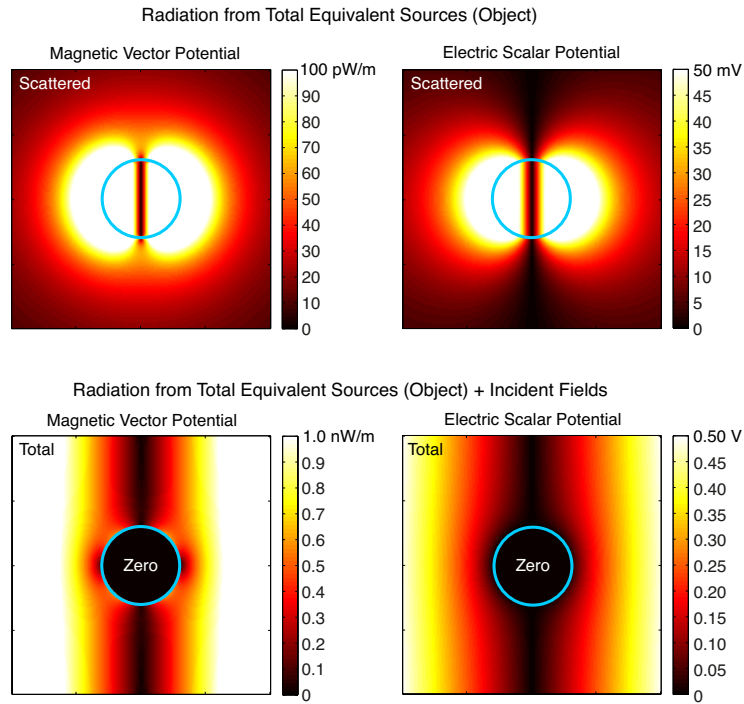
Figure 4.5: Potentials created by equivalent sources on the object obtained by using PIEs for a single sphere.
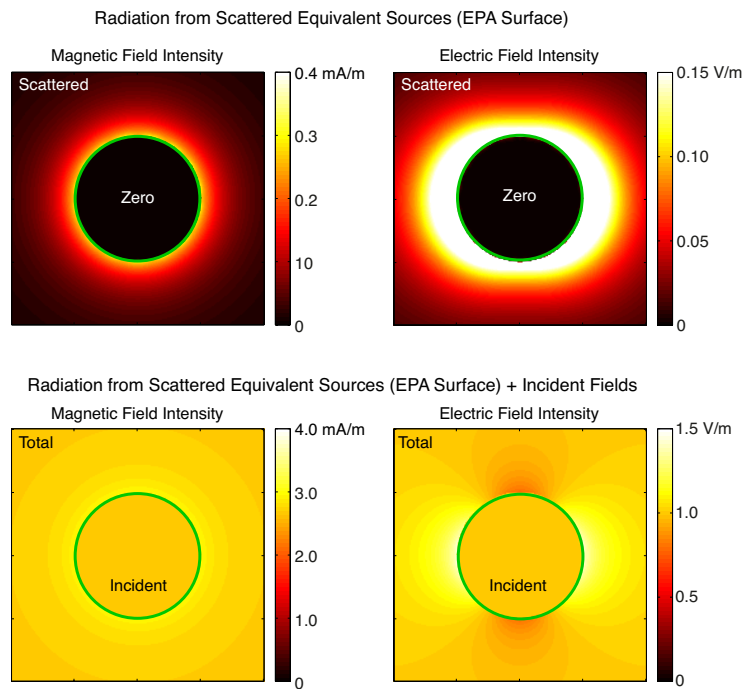

Figure 4.6: Fields created by equivalent sources on the ES obtained by using EPA-PIE for a single sphere.
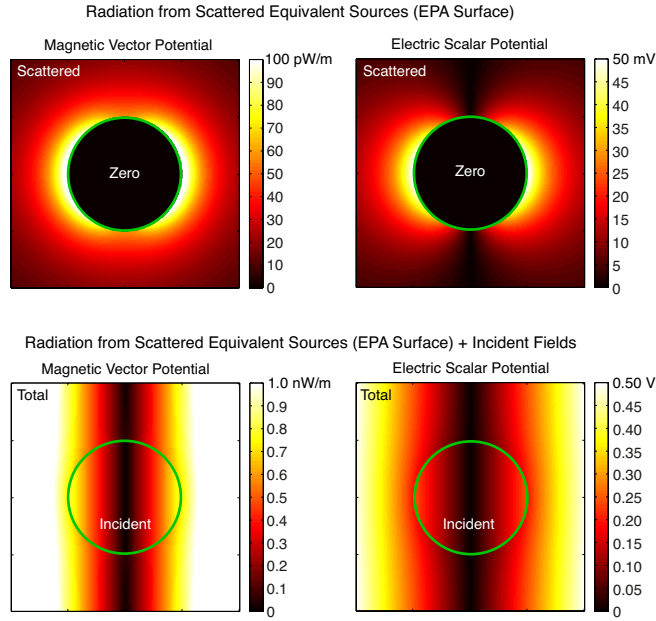
Figure 4.7: Potentials created by equivalent sources on the ES obtained by using EPA-PIE for a single sphere.

For a single domain problem, there is no need for a translation operator and only the scattering operator is used. Hence, we consider a $2 \times 2 \times 2$ array of PEC spheres as the next set of examples. The dimensions of the objects and ESs, as well as the excitation, are similar to those in the previous example. The periodicity in all directions is 0.6 m. Figures 4.8a and 4.8b depict far-zone electric field intensity for GMRES tolerance of 10^{-3} and 10^{-5} at 1 MHz and 10 kHz. The number of iterations for EFIE, PIE, and EPA-PIE is equal to 95, 389, and 6, respectively, for the residual error of 10^{-5}. It can be observed that, EFIE fails to find accurate results at the lower frequencies, while EPA-PIE and PIE are always consistent with each other. At the higher frequencies, EFIE can be forced to be accurate by reducing the residual error of the iterations, while this is not a feasible solution.
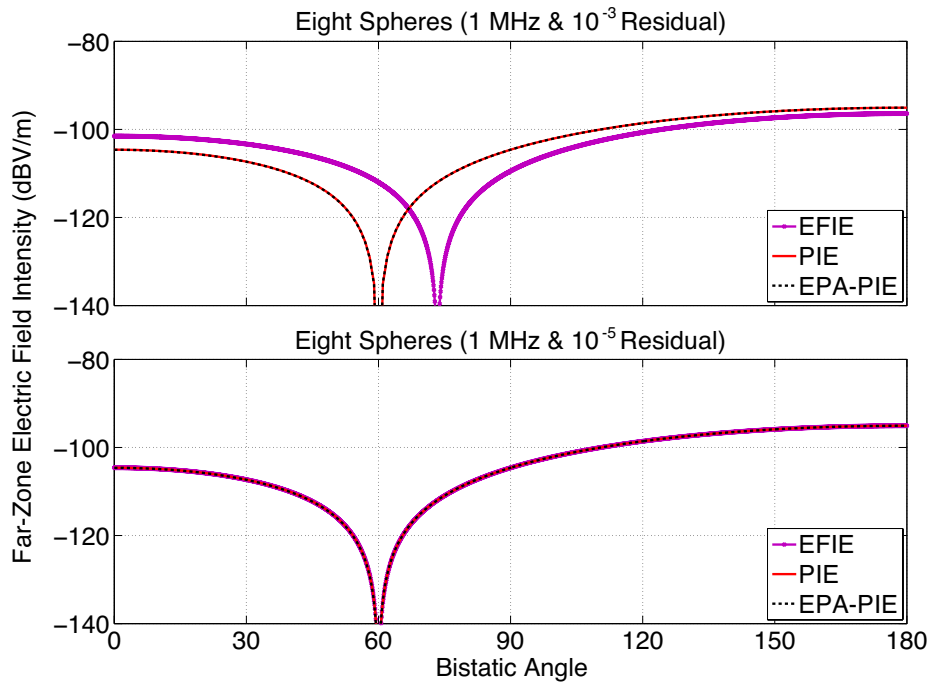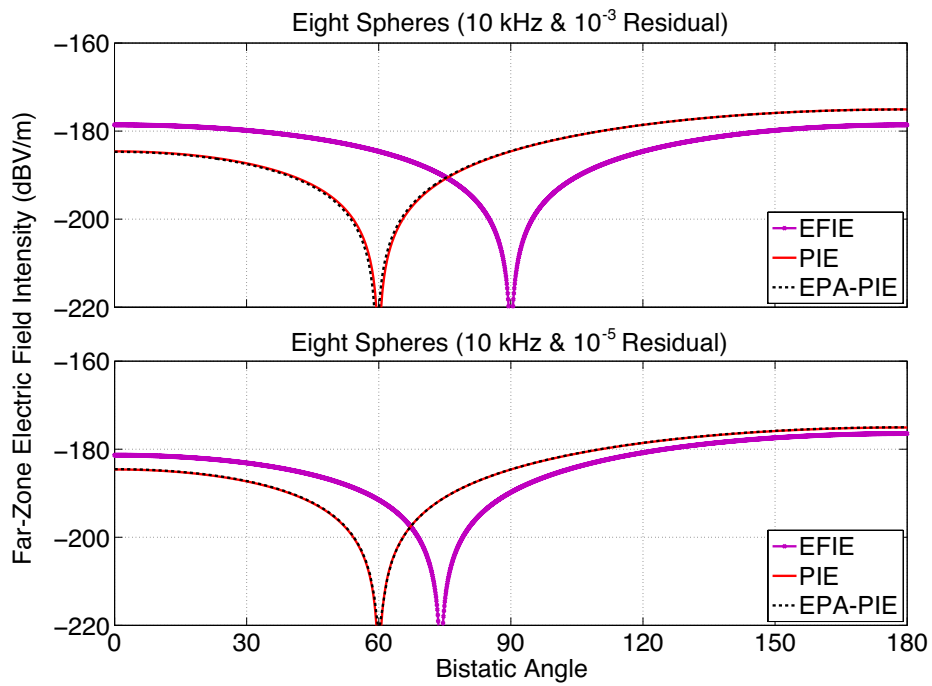
Figure 4.8: Solutions of scattering problem involving a $2 \times 2 \times 2$ array of PEC spheres at (a) 1 MHz and (b) 10 kHz.

CHAPTER 5

CONCLUSION

In this thesis, EPA implementations are developed to solve electromagnetic scattering problems involving PEC and penetrable objects of arbitrary shapes. Field projections are performed by using the identity operator (NEPA) and integro-differential operators (TEPA). It is shown that the error of EPA solutions is controllable by means of equivalence surface definitions and their discretization. Based on numerical examples, it is observed that EPA can increase the efficiency of solutions by reducing the number of unknowns, and particularly by enhancing the conditioning of matrix equations in comparison to standard solutions with MoM implementations. It is further shown that EPA becomes even more efficient for array structures with identical elements, since scattering and translation operators can be reused without repetitive calculations. EPA can also be hybridized with fast and/or asymptotic algorithms, such as MLFMA and physical optics.

As the major novelty of this thesis, we present the application of EPA to recently developed PIEs. In order to avoid low-frequency breakdown, PIEs have been introduced in the literature, especially to solve challenging problems involving dense discretizations with respect to wavelength. In order to incorporate PIEs to EPA, the equivalence equations are updated by including all quantities, including potentials. The developed EPA-PIE implementation enables fast, accurate, and stable solutions of dense discretizations without any numerical breakdowns.

REFERENCES

[1] Ö. Ergül and L. Gürel, *The multilevel fast multipole algorithm (MLFMA) for solving large-scale computational electromagnetics problems.* John Wiley & Sons, 2014.

[2] W. C. Chew, E. Michielssen, J. Song, and J.-M. Jin, *Fast and efficient algorithms in computational electromagnetics.* Artech House, Inc., 2001.

[3] P. Ylä-Oijala, M. Taskinen, and S. Järvenpää, "Surface integral equation formulations for solving electromagnetic scattering problems with iterative methods," *Radio Science*, vol. 40, pp. 1–19, Dec 2005.

[4] M. K. Li and W. C. Chew, "Wave-field interaction with complex structures using equivalence principle algorithm," *IEEE Transactions on Antennas and Propagation*, vol. 55, pp. 130–138, Jan 2007.

[5] M. K. Li and W. C. Chew, "Multiscale simulation of complex structures using equivalence principle algorithm with high-order field point sampling scheme," *IEEE Transactions on Antennas and Propagation*, vol. 56, pp. 2389–2397, Aug 2008.

[6] H. Shao, J. Hu, and W. C. Chew, "Solving array structures using single-source equivalence principle algorithm," in *2013 International Conference on Electromagnetics in Advanced Applications (ICEAA)*, pp. 774–777, Sept 2013.

[7] K. Zhang, J. Ou Yang, F. Yang, C. Wu, Y. Li, and J. Zhang, "Radiation analysis of large antenna array by using periodic equivalence principle algorithm," *Progress In Electromagnetics Research*, vol. 136, pp. 43–59, 2013.

[8] H. Shao, J. Hu, W. Lu, H. Guo, and Z. Nie, "Analyzing large-scale arrays using tangential equivalence principle algorithm with characteristic basis functions," *Proceedings of the IEEE*, vol. 101, pp. 414–422, Feb 2013.

[9] M. Fallahpour and W. C. Chew, "Equivalence principle algorithm for analysis of metamaterials and reconfigurable pixelled antennas," in *Antennas and Propagation and USNC/URSI National Radio Science Meeting, 2015 IEEE International Symposium on*, pp. 961–962, IEEE, 2015.

[10] H. Shao, J. Hu, Z.-P. Nie, G. Han, and S. He, "Hybrid tangential equivalence principle algorithm with MLFMA for analysis of array structures," *Progress In Electromagnetics Research*, vol. 113, pp. 127–141, 2011.

[11] K. Zhang, J. Ouyang, F. Yang, J. Zhang, and W. Luo, "Radiation pattern simulation of antenna array problem with perfectly electrically conducting object in arbitrary shape using novel hybrid method of equivalence principle algorithm and physical optics," *IET Microwaves, Antennas Propagation*, vol. 8, pp. 217–227, March 2014.

[12] Q. S. Liu, S. Sun, and W. C. Chew, "An integral equation method based on vector and scalar potential formulations," in *Antennas and Propagation & USNC/URSI National Radio Science Meeting, 2015 IEEE International Symposium on*, pp. 744–745, IEEE, 2015.

[13] W. C. Chew, "Vector potential electromagnetics with generalized gauge for inhomogeneous media: formulation," *Progress In Electromagnetics Research*, vol. 149, pp. 69–84, 2014.

[14] F. Vico, M. Ferrando, L. Greengard, and Z. Gimbutas, "The decoupled potential integral equation for time-harmonic electromagnetic scattering," *Communications on Pure and Applied Mathematics*, vol. 69, no. 4, pp. 771–812, 2016.

[15] Q. S. Liu, S. Sun, and W. C. Chew, "A potential-based integral equation method for low-frequency electromagnetic problems," *IEEE Transactions on Antennas and Propagation*, vol. 66, pp. 1413–1426, March 2018.

[16] U. M. Gür and Ö. Ergül, "Accuracy of sources and near-zone fields when using potential integral equations at low frequencies," *IEEE Antennas and Wireless Propagation Letters*, vol. 16, pp. 2783–2786, 2017.

[17] U. Gür, B. Karaosmanoğlu, and O. Ergül, "Solutions of new potential integral equations using approximate stable diagonalization of the green's function," in *Electromagnetics in Advanced Applications (ICEAA), 2017 International Conference on*, pp. 1894–1897, IEEE, 2017.

[18] C. Balanis, *Engineering Electromagnetics*. Wiley, 1989.

[19] W. C. Chew, M. S. Tong, and B. Hu, "Integral equation methods for electromagnetic and elastic waves," *Synthesis Lectures on Computational Electromagnetics*, vol. 3, no. 1, pp. 1–241, 2008.

[20] P. Ylä-Oijala, M. Taskinen, and S. Järvenpää, "Analysis of surface integral equations in electromagnetic scattering and radiation problems," *Engineering Analysis with Boundary Elements*, vol. 32, no. 3, pp. 196–209, 2008.

[21] Ö. Ergül and L. Gürel, "Stabilization of integral-equation formulations for the accurate solution of scattering problems involving low-contrast dielectric objects," *IEEE Transactions on Antennas and Propagation*, vol. 56, pp. 799–805, March 2008.

[22] P. Ylä-Oijala and M. Taskinen, "Electromagnetic scattering by large and complex structures with surface equivalence principle algorithm," *Waves in Random and Complex Media*, vol. 19, no. 1, pp. 105–125, 2009.

[23] B. Karaosmanoğlu, A. Yılmaz, and . Ergül, "A comparative study of surface integral equations for accurate and efficient analysis of plasmonic structures," *IEEE Transactions on Antennas and Propagation*, vol. 65, pp. 3049–3057, June 2017.

[24] H. İbili, B. Karaosmanoğlu, and Ö. Ergül, "Demonstration of negative refractive index with low-cost inkjet-printed microwave metamaterials," *Microwave and Optical Technology Letters*, vol. 60, no. 1, pp. 187–191, 2018.

[25] F. Mutlu, C. Önol, B. Karaosmanoğlu, and Ö. Ergül, "Inkjet-printed cage-dipole antennas for radio-frequency applications," *IET Microwaves, Antennas & Propagation*, vol. 11, no. 14, pp. 2016–2020, 2017.

[26] Z. G. Qian and W. C. Chew, "A quantitative study on the low frequency breakdown of EFIE," *Microwave and Optical Technology Letters*, vol. 50, pp. 1159–1162, May 2008.

[27] L. E. Sun, M. K. Li, and W. C. Chew, "Applying the low frequency technique to the equivalence principle algorithm," in *2009 IEEE Antennas and Propagation Society International Symposium*, pp. 1–4, June 2009.

[28] L. Sun, W. Chew, and J. Jin, "Augmented equivalence principle algorithm at low frequencies," *Microwave and Optical Technology Letters*, vol. 52, no. 10, pp. 2274–2279, 2010.